FISFVIFR

Contents lists available at ScienceDirect

Journal of Fluids and Structures

iournal homepage: www.elsevier.com/locate/ifs



Experimental and theoretical correlations for energy harvesting from a large flapping flag response



D.M. Tang, Dani Levin, E.H. Dowell *,1

Department of Mechanical Engineering and Materials Science, Duke University, Durham, NC 27708-0300, USA

ARTICLE INFO

Article history: Received 18 February 2019 Accepted 21 February 2019 Available online 7 March 2019

ABSTRACT

Two experimental models are constructed, i.e. partially covered and fully covered, cantilevered plates with piezoelectric piezo patches and film sensors. Two different experimental methods are used to obtain large flapping vibrations, a mechanically forced vibration and a limit cycle oscillation from an aeroelastic responses. AC voltage outputs from the piezo patch or film sensors and a DC power extraction through a AC/DC converter circuit are obtained. These experiments are used to evaluate a new computational model and code for a piezoelectric-aeroelastic system.

© 2019 Elsevier Ltd. All rights reserved.

1. Introduction

Recently energy harvesting from a large nonlinear aeroelastic response has been studied theoretically and experimentally. An inextensible beam and plate theory developed by Simmonds and Libai (1981) and Darmon and Benson (1986) and an alternate approach developed by Tang et al. (2014) have provided a strong theoretical foundation. In the present paper, this latter approach has been applied to nonlinear aeroelastic response analysis and aero-electromechanical coupling model analysis and also correlated with results from wind tunnel experiments.

Based on the limit cycle oscillations (LCO) of a fluttering plate, an aeroelastic energy harvester can be created for piezoelectric power generation in an aerodynamic flow field. Dunnmon et al. (2011) studied power extraction using a flexible plate with piezoelectric laminates that is self excited by a uniform axial flow field in a manner analogous to a flapping flag. Dunnmon's computational code used an inextensible beam theory with a linear vortex-lattice aerodynamic model and a linear electric circuit model, but the effect of the stiffness and mass created by the piezoelectric sheet mounted on both sides of the flag surface on the flag structural dynamics was not considered.

Tang and Dowell (2018) have studied nonlinear aeroelastic response and energy harvesting of a piezoelectric laminated plate based on an inextensible plate theory, Tang and Dowell (2014). The laminated plate is rotated from a position with the clamped edge normal to the flow (0 degree) to where the clamped edge is aligned with the flow (90 degree), i,e the yaw angle, β , varies from 0° to 180°. The structural dynamics of the piezoelectric laminated plate and also the electric-mechanical coupling dynamics are considered in this paper. One creates the aeroelastic model by coupling a newly developed inextensible nonlinear plate structural model and an electromechanical model with a rotated vortex lattice aerodynamic model. Also this research includes a study of the effect of the yaw angle and the resistive load on the electric power extraction and the LCO itself for the piezoelectric laminated plate.

E-mail address: dowell@ee.duke.edu (E.H. Dowell).

^{*} Corresponding author.

William Holland Hall Professor.

The current research focuses on theoretical and experimental correlation both for the flapping response and energy harvesting. The structural dynamic equation includes the effect of the mass and stiffness of piezoelectric sheets, A finite element method (FEM) of a beam is used to determine the eigenvalue and eigenvector of this structural system. Two cases of the theoretical and experimental correlation are considered. One is an experiment for a large flapping response created by an external force vibration excitation near the second bending natural frequency. This experiment not only evaluates the theoretical aero-electromechanical coupling model, but also the nonlinear inextensible beam theory when the electric circuit is closed. Another experiment is for a large flapping response created by a limit cycle oscillation (LCO) of a fluttering flag providing an aeroelastic energy harvester created for piezoelectric power generation in an aerodynamic flow field.

To place the present work in the context of a broader range of studies on energy harvesting, the reader may wish to first consult the paper by Li et al. (2016). This wide ranging review paper with 184 references provides an overview and critical assessment of energy harvesting by means of flow-induced vibrations on aerospace vehicles for a number of distinct system geometries and distinct physical mechanisms. It includes a discussion of energy harvesting by flapping geometries as discussed in the present paper. More specifically, the paper by Wang et al. (2016) is a theoretical/computational study of the geometry and physical mechanism discussed in the present paper and emphasizes the advantages of matching the resonant frequency of the cantilevered plate structure with the resonant frequency of the electrical circuit to achieve greater energy harvesting. Finally, in two papers by Kim et al. (2013) and Ryu et al. (2015), the inverted flag configuration is studied. In these two papers the flow direction is from the free end of a cantilevered plate toward the clamped end, as distinct from the present paper where the flow is from the clamped end toward the free end. The physical mechanism that leads to mechanical vibrations of the flag or cantilevered plate is quite different in the inverted flag versus what we will call the standard flag. As will be seen in this paper, for the standard flag configuration, the plate becomes dynamically unstable above a certain critical flow velocity and a limit cycle oscillation (LCO) of increasing amplitude is obtained for flow velocities above the critical value. The amplitude of the LCO increases smoothly from zero starting at the critical flow velocity. By contrast for an inverted flag the cantilevered plate has a static instability at a much lower flow velocity, but then there is no oscillation of the flag for larger flow velocities until the shape is sufficiently large that a strong oscillating flow vortex is created analogous to a Von Karman vortex street behind a bluff body. The statically deformed plate effectively becomes a bluff body when the static deformation becomes sufficiently large. Both flag configurations are of interest and have their relative advantages and disadvantages, but the physical mechanisms that produce mechanical vibrations and the opportunities for energy harvesting are quite different.

2. Experimental model and measurement system

2.1. Experimental model for partly covered piezoelectric patch and piezo film sensors

A 6061-T6 aluminum elastic plate was used as a substrate lamination. One end was clamped to a heavy support that was fixed on the ground and the other end is free. Two kinds of piezoelectric patches, P-876A12 and piezo film sensors, DT2-028K/L, DT4-028K/L were bonded to the substrate on both surfaces or only on one surface. A schematic of the distribution of the piezoelectric patches and piezo film sensors is shown in Fig. 1. The material properties and geometry of the substrate laminate and the piezoelectric patches and piezo film sensors are shown in Table 1.

2.2. Experimental model for fully covered piezo film sensors

The same cantilever elastic plate was used as a substrate, but twelve (12) piezo film sensors, DT4-028K/L were bonded to the substrate on both sides. A photograph of the distribution of the piezo film sensors is shown in Fig. 3.

The flexible plate has several piezoelectric patches and piezo film sensors attached and is placed in a uniform axial flow. This flexible system can be considered as a flapping flag model, i.e a non-uniform beam model. The stiffness and mass distributions are variable along the elastic axis. For the flag beam with two surface bonded P-876A12 piezoelectric patches, the equivalent bending stiffness is

$$EI_p = \frac{E_s t_s^3 b}{12} + \frac{2E_p t_p b_p}{3} (\frac{3}{4} t_s^2 + \frac{3}{2} t_p t_s + t_p^2) = EI_s + \frac{2E_p t_p b_p}{3} (\frac{3}{4} t_s^2 + \frac{3}{2} t_p t_s + t_p^2)$$

and the equivalent mass per length is

$$m_p = \rho_s b t_s + 2\rho_p b_p t_p = m_s + 2\rho_p b_p t_p$$

where $EI_s = \frac{E_s t_s^3 b}{12}$ and $m_s = \rho_s b t_s$. For the flag beam with one surface bonded TD2-028/K/L or TD4-028K/L piezo film sensor, the equivalent bending

$$EI_t = EI_s + \frac{E_t t_t b_t}{3} (\frac{3}{4} t_s^2 + \frac{3}{2} t_t t_s + t_t^2)$$

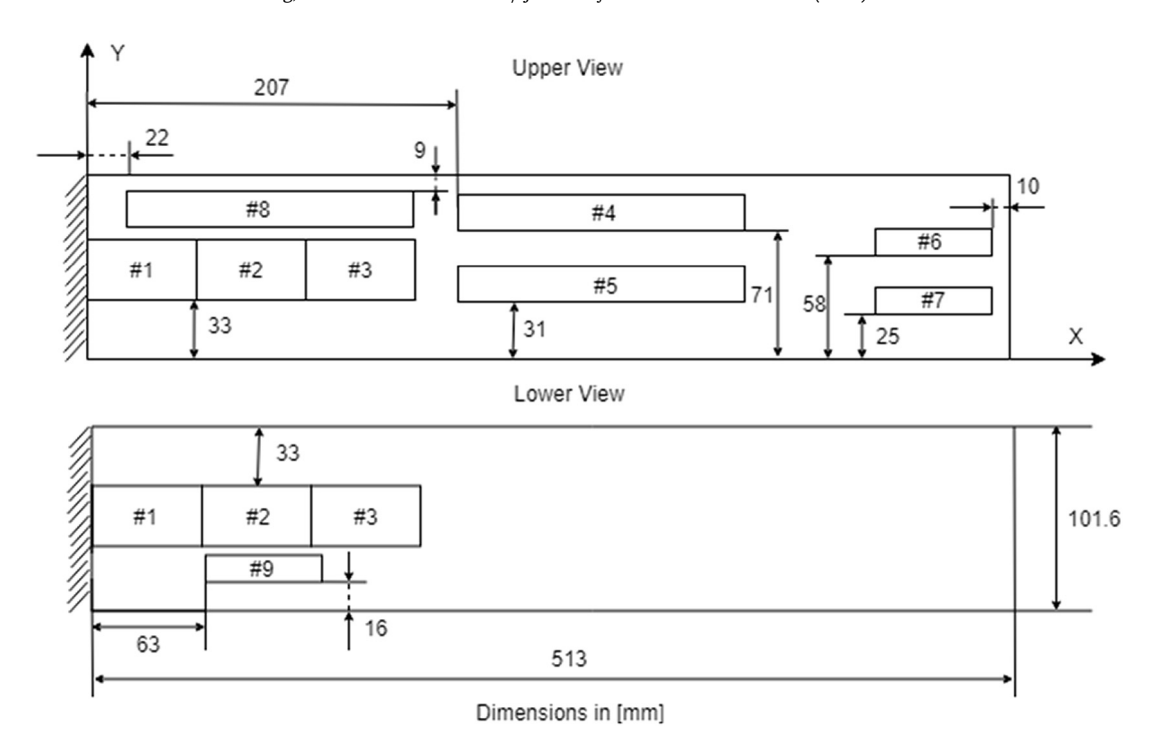


Fig. 1. Schematic of the distribution of the partly covered piezoelectric patches and piezo film sensors.

Table 1Geometric and material properties

Parameter	P-876A12	DT2-028K/L	DT4-028K/L	Substrate
Piezo-Sheet numbers,m	#1, 2, 3	#6, 7, 9	#4, 5, 8	1
Length (l_p, l_{t1}, l_{t2}, L) (mm)	61	73	171	513
Width (b_p, b_t, b) (mm)	35	16	16	101.6
Thickness (t_p, t_t, t_s) (mm)	0.5	0.04	0.04	0.375
Mass density (ρ_p, ρ_t, ρ_s) (kg/m^3)	4666	1789	1789	2840
Elastic modulus (E_p, E_t, E_s) (GPa)	23.3	3.0	3.0	68.9
Coupling coefficient (e_{31}^p, e_{31}^t) (C/m^2)	-0.6	-0.01	-0.01	
Permittivity constant $(\epsilon_{33}^p, \epsilon_{33}^t)$ (F/m)	$33.63e^{-9}$	$107e^{-12}$	$107e^{-12}$	

and the equivalent mass per length is

$$m_t = m_s + \rho_t b_t t_t$$

The flag stiffness and mass at any position along the x axis can determined from Fig. 1. For example, at x = 80 mm, the equivalent stiffness is

$$EI(x = 80) = EI_p + 2EI_t - EI_s$$

and the equivalent mass per unit length is

$$m(x=80)=m_p+m_t-m_s$$

The flag beam is divided into a finite number of elements connected to one another by nodes. The properties of the beam are assumed constant in each element. A standard finite element method (FEM) is used to calculate the eigenvalues and eigenvectors of this piezoelectric patch/beam system. The symmetric elemental mass and stiffness matrices are

$$[M_e] = \frac{m(x)l_e}{420} \begin{bmatrix} 156 & & & \\ 22l_e & 4l_e^2 & & \\ 54 & 13l_e & 156 & \\ -13l_e & -3l_e^2 & -22l_e & 4l_e^2 \end{bmatrix} \qquad [K_e] = \frac{EI(x)}{l_e^3} \begin{bmatrix} 156 & & & \\ 22l_e & 4l_e^2 & & \\ 54 & 13l_e & 156 & \\ -13l_e & -3l_e^2 & -22l_e & 4l_e^2 \end{bmatrix}$$

where l_e is the length of an element

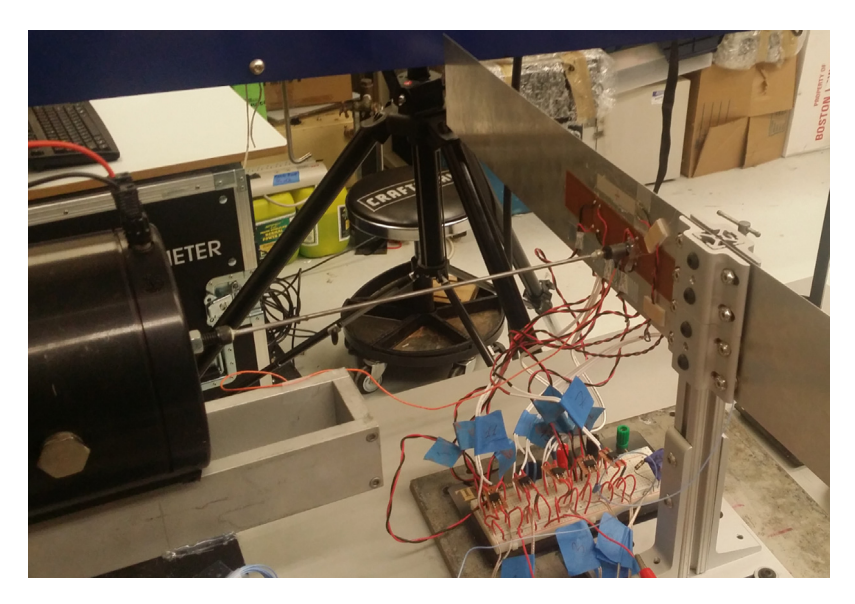


Fig. 2. Photograph of the forced vibration test setup.

2.3. Experimental setup and measurement data acquisition

In both cases the aluminum plate is cantilevered horizontally, flag configuration, from a stiff vertical aluminum profile. The data is acquired with m+p VibPilot 24bit 8ch DAQ. The AC voltages from piezo elements are rectified through full-wave DF04S rectifier. Tip acceleration is measured with PCB 352C22 accelerometer.

1. Dynamic responses and energy harvesting from a forced vibration test.

The plate is excited through *B*&*K* 4809 shaker, positioned horizontally and attached to the plate through Dytran 1022 V force sensor. The shaker is controlled through the DAQ unit with compatible amplifier. The applied force and tip acceleration are acquired directly. The excitation is pure sine with pre-set frequency. A photograph of the forced vibration test setup is shown in Fig. 2.

2. LCO aeroelastic response and energy harvesting from the wind tunnel test.

The cantilevered plate is placed inside the wind tunnel, with aluminum profile covered with 3d printed plastic shroud to reduce vortex shedding. Air speed is measured with a pitot tube sensor and acquired directly together with tip acceleration and voltage outputs in the DAQ unit. The air speed is increased manually with data recorded constantly during the tests. The tip deflection was measured with an accelerometer and the deflection inferred from that. Given a dominant single frequency in the response, this is straightforward. A photograph of the aeroelastic model (fully covered model) in the wind tunnel is shown in Fig. 3.

3. Fluid-electromechanical equations of motion

Using a Rayleigh-Ritz approach, one can expand the transverse deflection, w, of the beam as follows:

$$w = \sum_{i} q_i(t)\phi_i(x) \qquad , \qquad i = 1, \dots, nx$$
 (1)

where $\phi_i(x)$ are the natural mode functions of the transverse deflection of the cantilevered beam calculated from FEM. These functions satisfy the geometric boundary conditions of the cantilevered beam. q_i is the generalized coordinate of beam associated with the ith eigenmode, nx is the total mode number used in the computations.

3.1. Potential energy

The structural potential energy for an inextensible beam is given by:

$$U_b = \frac{1}{2} \int_0^L EI(x) \left(\frac{\partial^2 w}{\partial x^2}\right)^2 \left[1 + \left(\frac{\partial w}{\partial x}\right)^2\right] dx \tag{2}$$

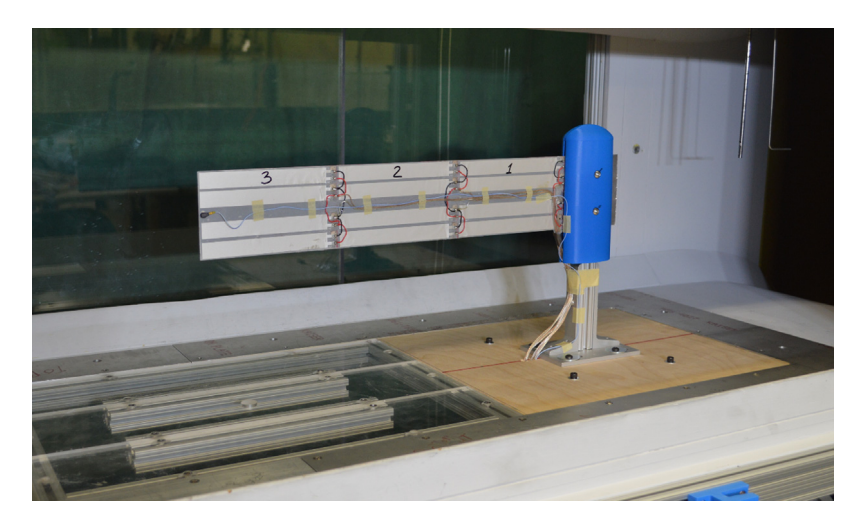


Fig. 3. Photograph of the aeroelastic model (fully covered model) in the wind tunnel.

From Stanton et al. (2010), the electric potential for each piezo sheet is given by

$$U_e = -\frac{1}{2}CV^2 = -\frac{1}{2}C\dot{\lambda}^2 \tag{3}$$

where *C* is the series capacitance of both piezoelectric sheets. λ , is a flux linkage coordinate and the sign of the field is opposite for the upper and lower piezo sheets. Here $\dot{\lambda} \equiv V$ and *V* is the voltage.

Thus the total conservative potential energy through each piezo sheet and an inextensible elastic beam is given by:

$$U = U_b + U_e = \frac{1}{2} \int_0^L EI(x) \left(\frac{\partial^2 w}{\partial x^2}\right)^2 \left[1 + \left(\frac{\partial w}{\partial x}\right)^2\right] dx - \frac{1}{2} \sum_m^M C_m \dot{\lambda}_m^2 + \sum_m^M \Theta_m \dot{\lambda}_m \int_{x_m}^{x_m + l_m} \left(\frac{\partial^2 w}{\partial x^2}\right) \left[1 + \frac{1}{2} (\frac{\partial w}{\partial x})^2\right] dx$$

$$(4)$$

where

$$C_{m} = \begin{cases} \frac{\epsilon_{33}^{p_{3}}b_{p}l_{p}}{2t_{p}}, & m = 1, 2, 3\\ \frac{\epsilon_{33}^{t_{3}}b_{t_{2}}l_{1}}{t_{t}}, & m = 4, 5, 8\\ \frac{\epsilon_{33}^{t_{3}}b_{t_{1}}l_{2}}{t_{t}}, & m = 6, 7, 9 \end{cases}, \quad \Theta_{m} = \begin{cases} \frac{1}{2}E_{p}d_{31}^{p}b_{p}(t_{s} + t_{p}), & m = 1, 2, 3\\ \frac{1}{2}E_{t}d_{31}^{t}b_{t}(t_{s} + t_{t}), & m = 4 - 9 \end{cases}$$

where ϵ_{33}^p is the piezoelectric sheet permittivity of P-876A12 and ϵ_{33}^t is the piezo film sensor permittivity of DT2-028K/L abd DT4-028K/L. d_{31}^p is the piezoelectric constant of P-876A12 and d_{31}^t is the piezo film constant of DT2-028K/L abd DT4-028K/L

$$l_m = \begin{cases} l_p , & m = 1, 2, 3 \\ l_{t2} , & m = 4, 5, 8 \\ l_{t1} , & m = 6, 7, 9 \end{cases}$$

and x_m is the leading edge position of each piezoelectric sheet along the x axis. Details are shown in Fig. 1.

3.2. Kinetic energy

The kinetic energy of a cantilevered beam is given by

$$T_b = \frac{1}{2} \int_0^L m_b(x) (\dot{u}^2 + \dot{w}^2) dx \tag{5}$$

 $m_b(x)$ is the mass per unit length of the elastic beam.

For the inextensible beam theory, one may compute u as follows.

$$u(x,t) = -\frac{1}{2} \int_0^x \left(\frac{\partial w(\zeta,t)}{\partial \zeta} \right)^2 d\zeta$$

and thus

$$\dot{u}(x,t) = -\int_0^x \frac{\partial w(\zeta,t)}{\partial \zeta} \frac{\partial w^2(\zeta,t)}{\partial \zeta \partial t} d\zeta$$

Thus

$$T_b = \frac{1}{2} \int_0^L m_b(x) \left[\dot{w}^2 + \left(\int_0^x \frac{\partial w}{\partial \zeta} \frac{\partial w^2}{\partial \zeta \partial t} d\zeta \right)^2 \right] dx \tag{6}$$

3.3. Fluid-electromechanical equations of motion

To derive the equations of motion, Hamilton's principle requires the variation of the sum of the Lagrangian L = T - Uand nonconservative work terms to reach a stationary value between two instances in time, i.e

$$\int_{t_0}^{t_1} (\delta L + \delta W) dt = 0$$

where δ is a variational operator.

$$\delta L(\dot{w}, \dot{\lambda}_m, w'') = \frac{\partial L}{\partial \dot{w}} \delta \dot{w} + \frac{\partial L}{\partial \dot{\lambda}_m} \delta \dot{\lambda}_m + \frac{\partial L}{\partial w''} \delta w''$$
(7)

where $w^{''}\equiv \frac{\partial^2 w}{\partial x^2}$ The variation in the nonconservative work is

$$\delta W = -c_s \dot{w} \delta w + F_0 \sin(\omega t) \delta(x - x_f) \delta w + \Delta p(x, y, t) \Delta x \Delta y \delta w$$
(8)

where c_s is the beam structural damping coefficient, $\Delta p(x, y, t)$ is the aerodynamic pressure applied on the plate surface. F_0 is the external dynamic force amplitude, ω is a excitation frequency and x_f is the position of force applied.

Using Lagrange's equations for q_i and $\dot{\lambda}_i$ from Eqs.(7)–(8), the nonlinear fluid-electromechanical equations of motion for the inextensible beam are given as follows,

$$M_{bi}(\ddot{q}_i + 2\xi \omega_i \dot{q}_i + \omega_i^2 q_i) = F_0 \sin(\omega t)\phi_i(x_f) + Q_i + \sum_m \Theta_m \dot{\lambda}_m G 1_{i,m} - F_{BN} - F_{BM} + F_{EN}$$
(9)

$$C_m \ddot{\lambda}_m + \sum_i \Theta_m G \mathbf{1}_{i,m} \dot{q}_i = A_{\dot{q},m} \quad , \quad m = 1, ..M$$

where M_{bi} , ω_i and ξ_i are the generalized mass, the natural frequency and modal damping of the beam. $\sum_m \Theta_m \dot{\lambda}_m G 1_{i,m}$ is the linear electric induced force. Q_i is a generalized linear aerodynamic force. A linear vortex lattice aerodynamic model is used to calculate this aerodynamic force. The aerodynamic matrix equation is given by

$$[A]\{\Gamma\}^{t+1} + [B]\{\Gamma\}^t = \{w\}^{t+1},\tag{11}$$

where [A] and [B] are aerodynamic coefficient matrices, w_i^{t+1} is the downwash at the ith collocation point at time step t+1, Γ_j is the strength of the jth vortex. For a more detailed derivation of these aerodynamic equations, see Dunnmon et al. (2011) and Tang and Dowell (2018).

The structural nonlinear forces, F_{BN} , F_{BM} and the electric nonlinear force, F_{EN} are given as follows.

$$F_{BN} = \sum_{j} \sum_{k} \sum_{l} P5_{ijkl} (q_j q_k q_l)$$

$$F_{BM} = \sum_{j} \sum_{k} \sum_{l} M^p_{ijkl} \left[q_j q_k \ddot{q}_l + q_j \dot{q}_k \dot{q}_l + \dot{q}_j q_k \dot{q}_l \right]$$

$$F_{EN} = \sum_{m} \Theta_m \dot{\lambda}_m \sum_{i} \sum_{k} G2_{ijk,m} q_j q_k$$

and the current created by nonlinear structural deformation, $A_{q,m}$, is given by

$$A_{\dot{q},m} = \sum_{i} \sum_{j} \sum_{k} \Theta_{m} G2_{ijk,m} (\dot{q}_{i}q_{j}q_{k} + q_{i}\dot{q}_{j}q_{k} + q_{i}q_{j}\dot{q}_{k})$$

The coefficients $P5_{ijkl}$, M_{ijkl} and $G1_{i,m}$, $G2_{ijk,m}$ are given in Appendix.

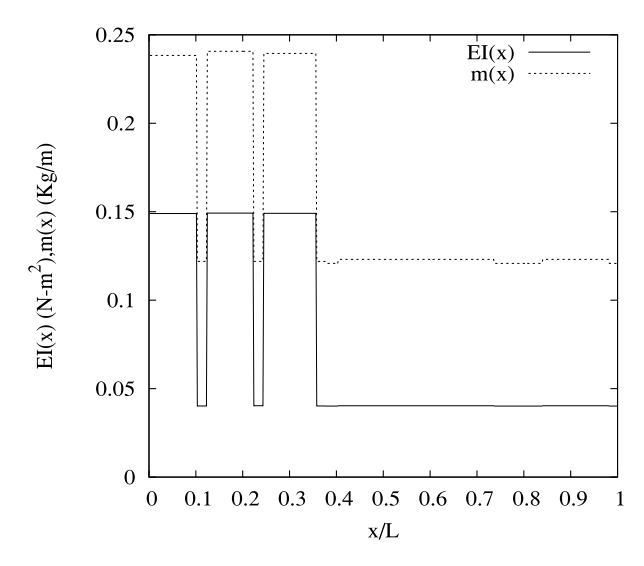


Fig. 4. Stiffness and mass per length distribution of the substrate flag including the piezoelectric patches and piezo film sensors.

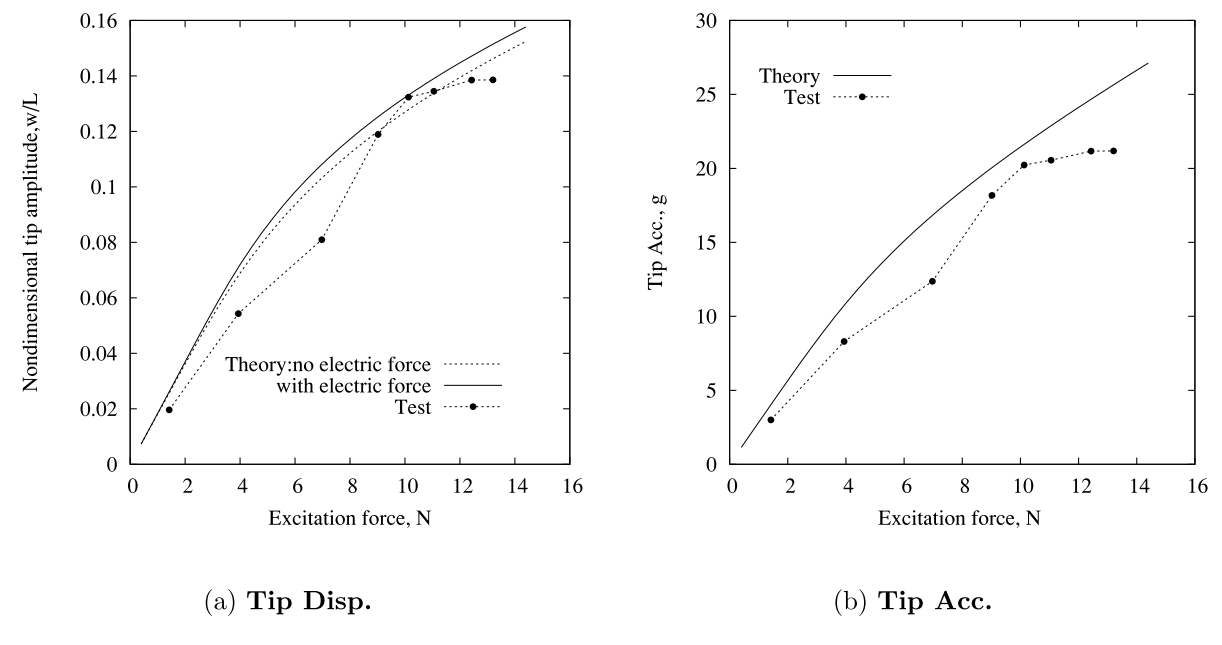


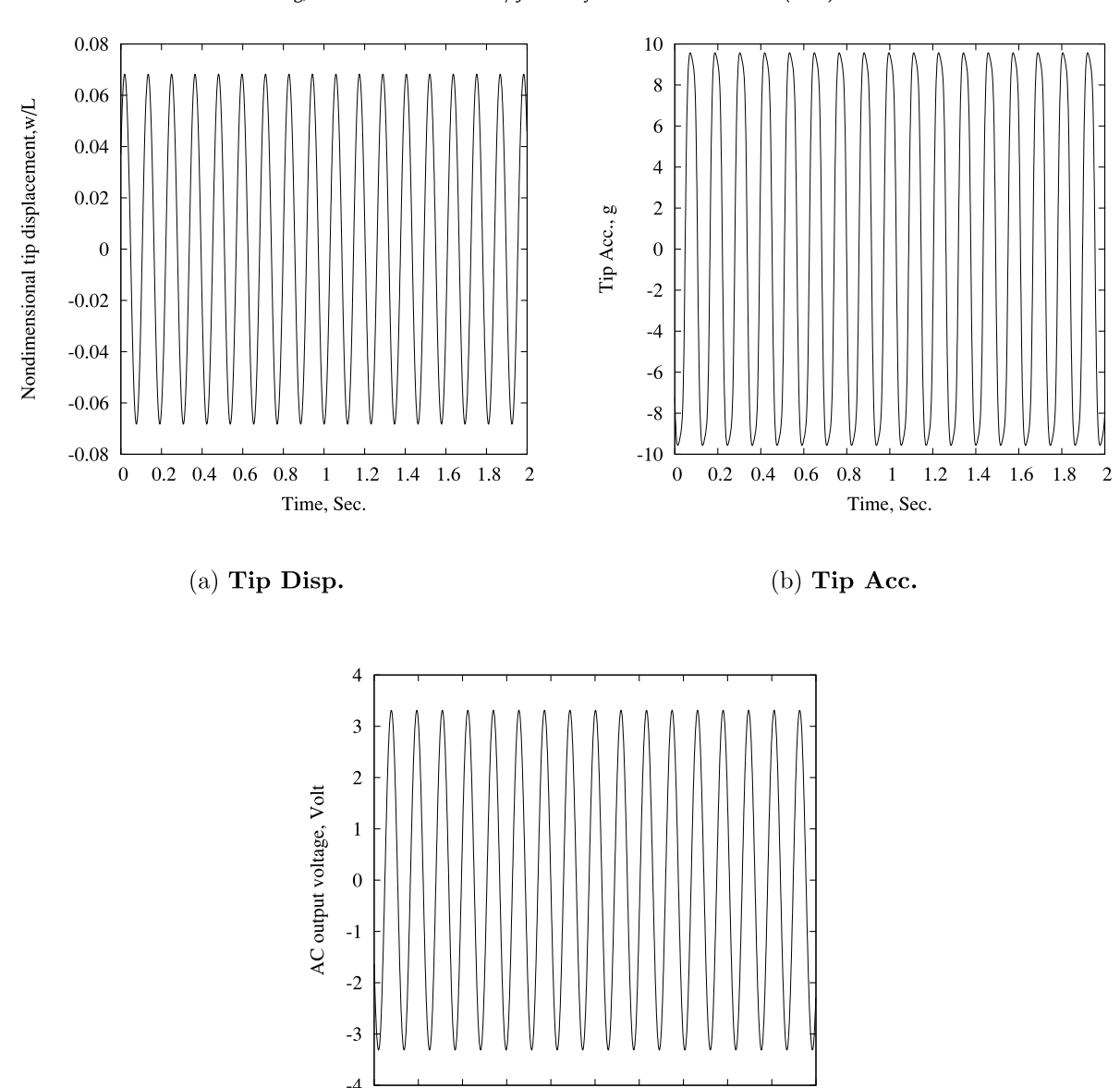
Fig. 5. Nondimensional peak tip amplitude, w_{tip}/L (a) and acceleration peak tip amplitude, g (b) vs external force from 0.4 N to 14.4 N.

4. Theoretical/Experimental Correlations

Fig. 4 shows the stiffness and mass per length distribution for the partly covered piezoelectric patch and piezo film sensors. The piezoelectric patch of P-876A12 provides a large additional stiffness and mass near the root of the cantilever beam. However the piezo film sensors of DT2-028 K/L and DT4-028K/L provide very small additional stiffness and mass. The weight of the accelerometers is accounted for in the computational model. The weight of the wires was added as distributed mass in the model. A FEM is used to calculate the eigenvalues and eigenvectors. The beam is divided into 100 finite elements. The first five (5) natural frequencies of the beam are 1.74, 8.67, 22.85, 45.53 and 73.73 Hz.

4.1. Dynamic response and power extraction from force vibration for partly covered plate model

A standard hammer test was performed in order to identify the dynamic properties of the experimental model. The first two natural frequencies are 1.23 and 8.6 Hz. An experimental model to be subjected to a dynamic loading was



(c) # **4 film**

0.8

0 0.2 0.4 0.6

Fig. 6. Time histories for the tip displacement, tip acceleration and output AC voltage from #4 film sensor for external force $f_0 = 4$ N.

1.2

.8 1 1 Time, Sec. 1.4 1.6 1.8

constructed. A periodic dynamic point force, $f_0 \sin(\omega t) \delta(x_f - L)$ is applied near the root of the cantilever beam, where ω is the external frequency and is set close to the experimental second natural frequency, 8.6 Hz. Note that the theoretical second natural frequency is 8.67 Hz. The force driving point is at x = 60 mm. Eqs. (9) and (10) are used to calculate the dynamic response and power extraction when the aerodynamic forces, Q_i , is set zero. First five bending modes are considered in the calculations and the modal damping is $\xi = 0.015$ for all modes. The external force f_0 varies from 0.4 N to 14.4 N.

Fig. 5(a) shows the nondimensional flap response amplitude, wtip/L at the tip for the external force amplitude from 0.4 N to 14.4 N for the theoretical computations and 1.42 N to 13.2 N for the experiment.

For comparison the results without the electric coupled equations [10] are also plotted in this figure. It is found that the nonlinear forces are dominated by those of the structure. The linear and nonlinear electric forces induced by the piezoelectric patch and film sensor are smaller. The correlation is reasonably good, but there are some differences between

1.6

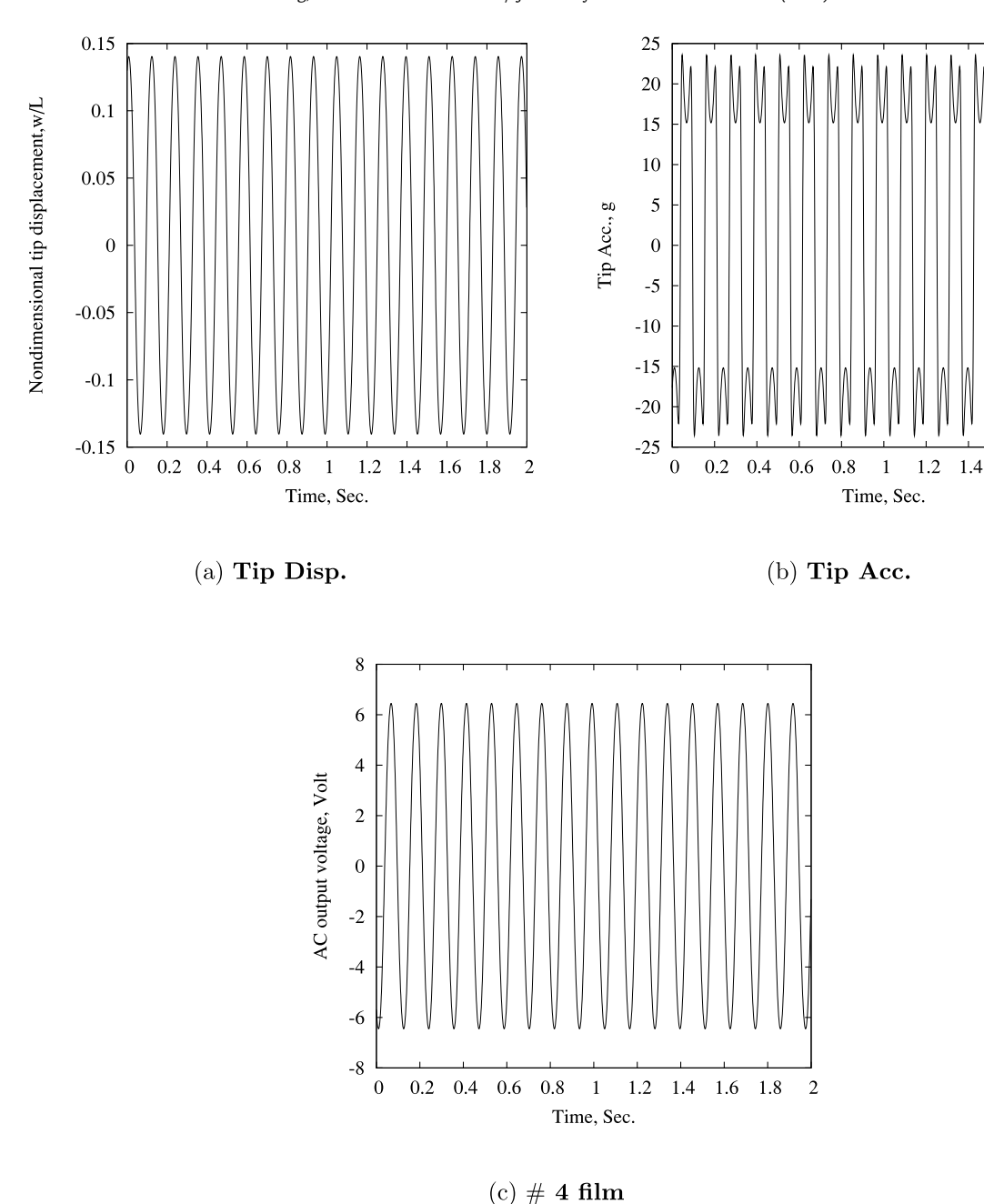


Fig. 7. Time histories for the tip displacement, tip acceleration and output AC voltage from #4 film sensor for external force $f_0 = 13.2$ N.

the computations and experiment. The source of the difference may come from both the computational model and the experimental measurement. The theoretical modal damping does not exactly match the experimental model, because it varies when the excitation frequency is equal to the second natural frequency. Also for the experimental measurement it is difficult to control the excitation frequency to be at exactly the second natural frequency. Although there are some differences, these results still provide a good experimental verification of the beam inextensible theory.

Fig. 5(b) shows the acceleration peak amplitude, g at the tip for the external force amplitude from 0.4 N to 14.4 N. The correlation is reasonably good. From the theoretical computations of the acceleration response, it is found that the nonlinear forces are dominated by the structural stiffness nonlinearity when the external force is larger. In addition to the dominant frequency component created by the excitation frequency, the response also includes a component at three (3) times the external frequency. For details, see Figs. 6–8 for the time histories and corresponding FFT analysis. Fig. 6 shows

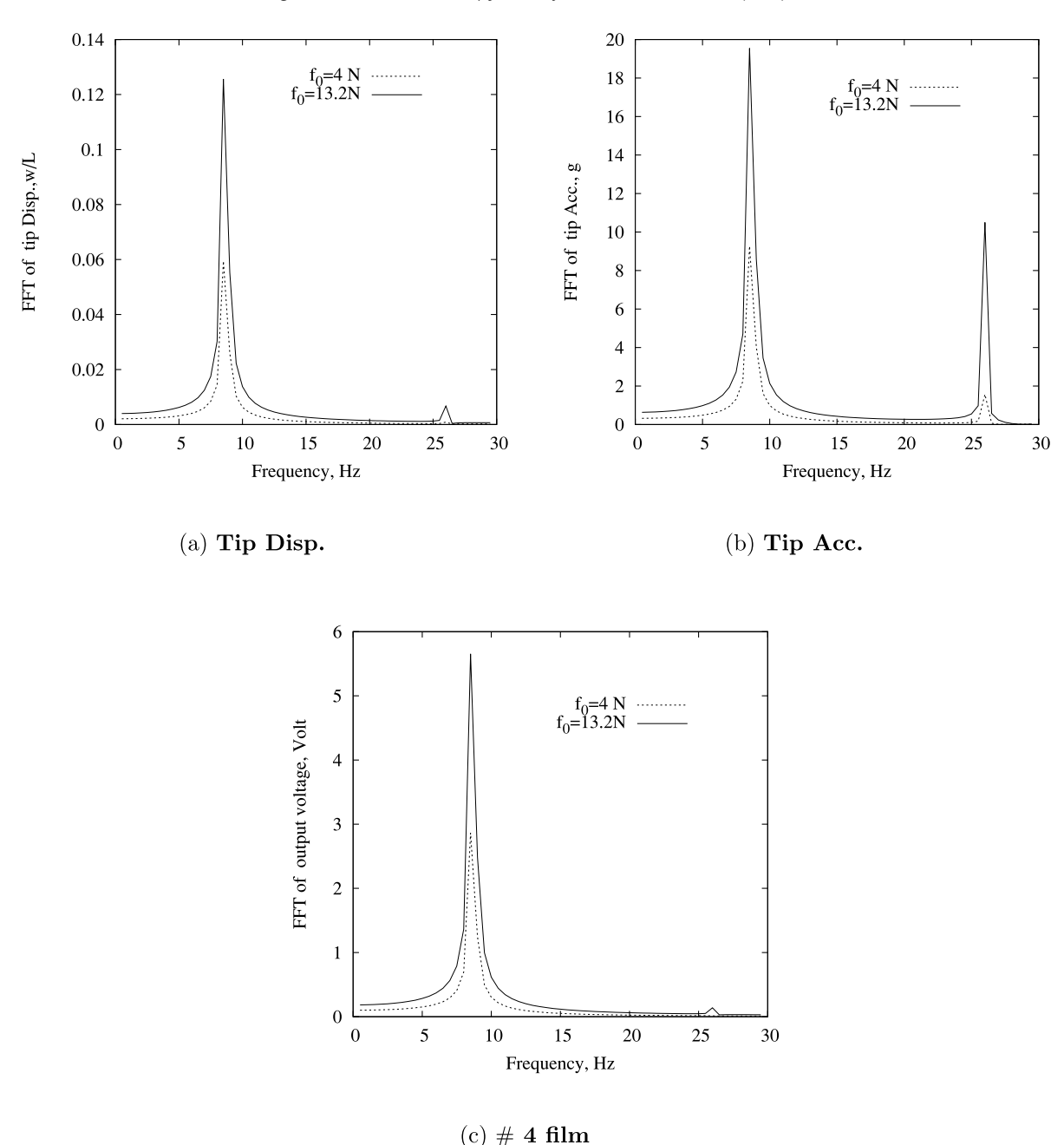


Fig. 8. FFT analysis of time histories for the tip displacement, tip acceleration and output AC voltage from #4 film sensor for external force $f_0 = 4$ and 13.2 N.

the time histories of the nondimensional tip displacement, tip acceleration and AC output voltage from # 4 film sensor for a small external force, $f_0 = 4$ N. It is found that the effect of structural nonlinearity is very small. For the same case for a large external force, $f_0 = 13.2$ N, the nonlinear structural effect becomes larger as shown in Fig. 7. Fig. 8 shows the FFT analysis for both small and large external forces. The higher harmonic component with $3 \times \omega_f$ frequency increases as the external force increases. The results from Figs. 6–8 are all from the computational model.

The theoretical output sinusoidal voltage signal generated from the piezoelectric patch converts to a DC voltage through an AC/DC converter circuit and is directly connected with the capacitor. For the detailed algorithm of this conversion, see Wang and Wu (2012). The algorithm is based on the assumption that the external electric circuit has a small effect on the voltage output of the piezoelectric patch, and hence the amplitude of the voltage output on the patch remains unchanged during the charging process. The DC amplitude remains the AC amplitude.

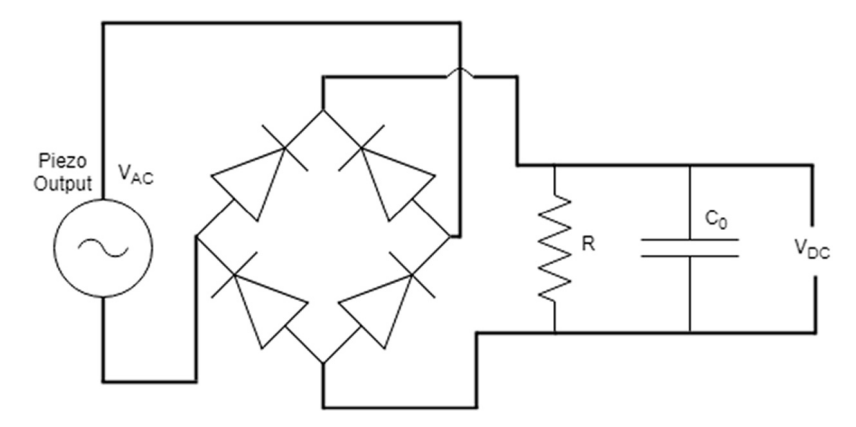


Fig. 9. Schematic of AC/DC converter circuit of the experiment. R is an effective resistance and C_0 is a capacitance, $C_0 = 22 \, \mu F$.

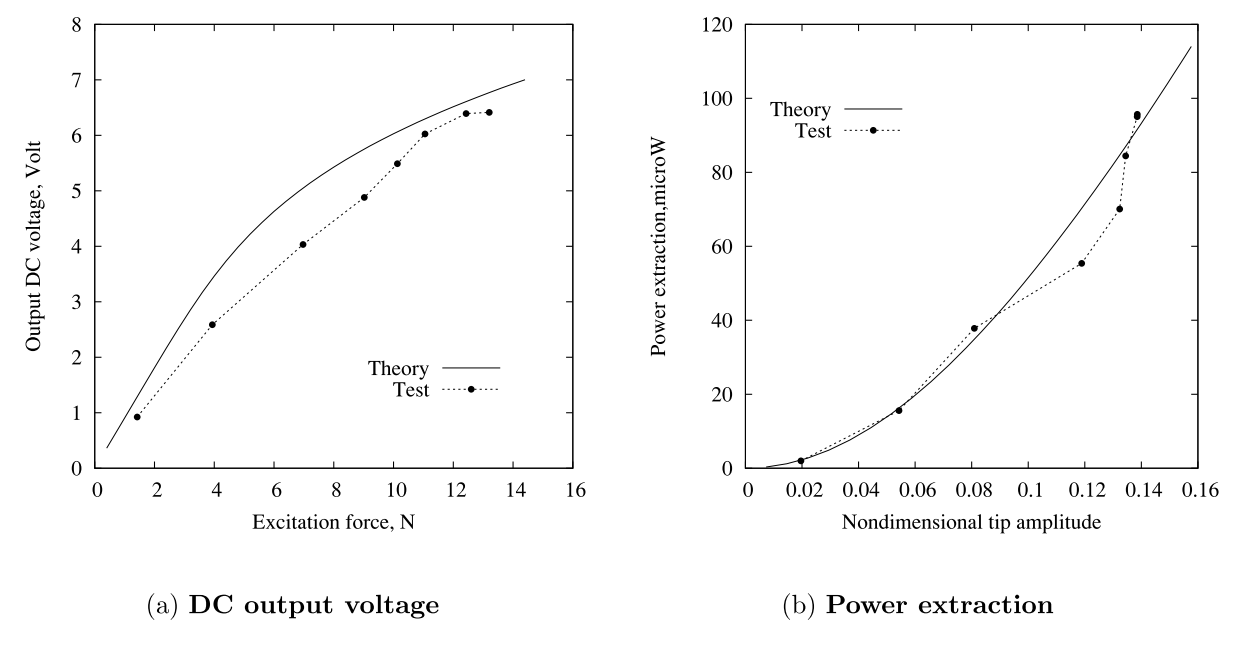


Fig. 10. Output DC voltage (a) and power extraction (b) from #4 piezo film sensor.

The experimental output voltage signal generated from the piezoelectric patch converts to a DC voltage through an AC/DC converter circuit. The electric circuit is shown in Fig. 9.

Fig. 10(a) shows the DC output voltage at #4 piezo film sensor and the external force amplitude from 0.4 N to 14.4 N. As expected the DC output voltage increases as the external force increases. The correlation is reasonably good, but there are some differences between the computations and experiments. The source of the error may come from the determination of the piezoelectric properties such as the coupling constants, e_{31}^p , e_{31}^t and permittivity constants, e_{33}^p , e_{33}^t . Here the piezo film coupling constant is obtained from the experimental tip response and the corresponding AC output voltage using the linear electric equation. The experimental conversion of the AC to DC signal is not the ideal assumed in the computational model. But this difference does not explain all of the difference between computed and measured power generation. Also the generated AC voltage from the piezo film sensor is close to the converted DC voltage. The experimental conversion of the AC to DC signal is not the ideal assumed in the computational model. But this difference does not explain all of the difference between computed and measured power generation.

Corresponding to this output voltage of the #4 film sensor, the power extraction can be calculated as

$$P_{DC} = V_{DC}^2/R$$

where R is an effective resistance, R = 430 k Ohm.

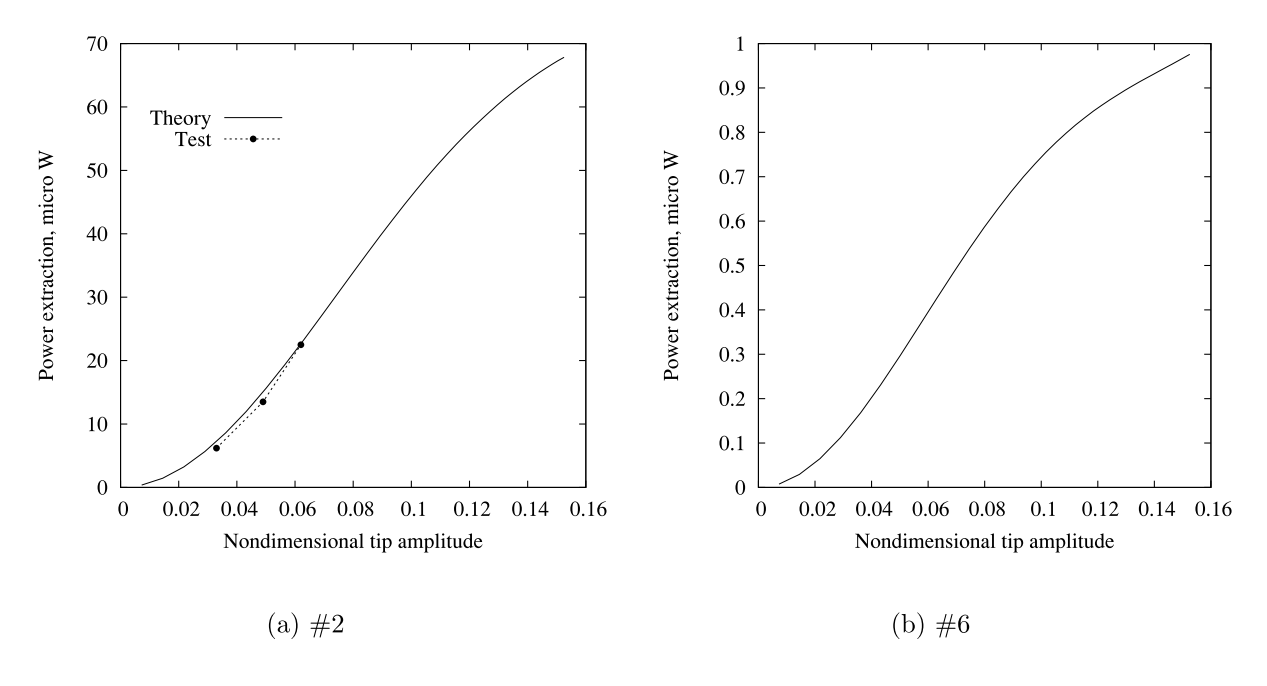


Fig. 11. Power extraction from piezoelectric patch at #2 (a) and piezo film sensor at #6 (b).

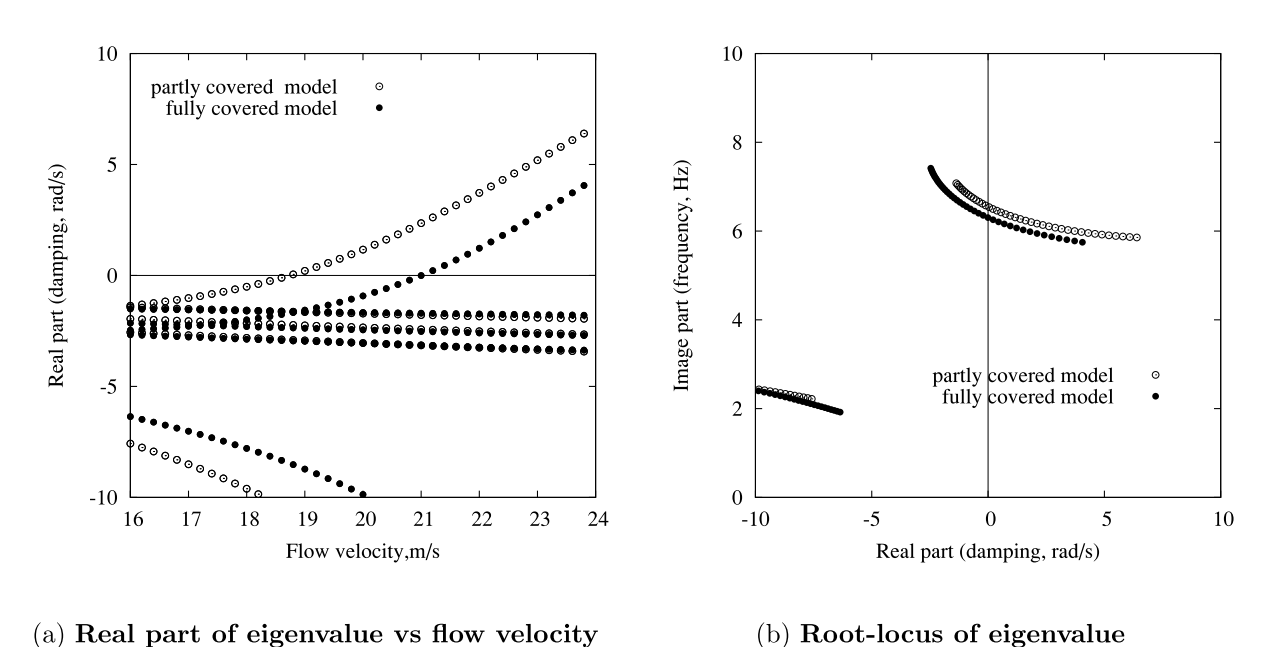


Fig. 12. Graphical representation of the eigenvalue.

The results are shown in Fig. 10(b). The correlation is good.

For the other piezoelectric patch and film sensors, such as #1-3 and #6, #7 elements, the power extraction is also computed. Two typical elements are shown in Fig. 11(a) and (b). Fig. 11(a) shows the power output for piezoelectric patch, P-876A12 at #2 and 11(b) shows the theoretical results for film sensor, DT2-028K/L at #6. Because the #5 of the piezo film sensor has the same position as #4 in x direction, the output voltage of #5 is the same as that of #4. If #4 and #5 film sensors are connected in parallel, then the output power will double. The above conclusion is also similar for #6 and #7. Comparing Fig. 10 to Fig. 11, it is found that the elements of #4 or #4+#5 provide a better power extraction.

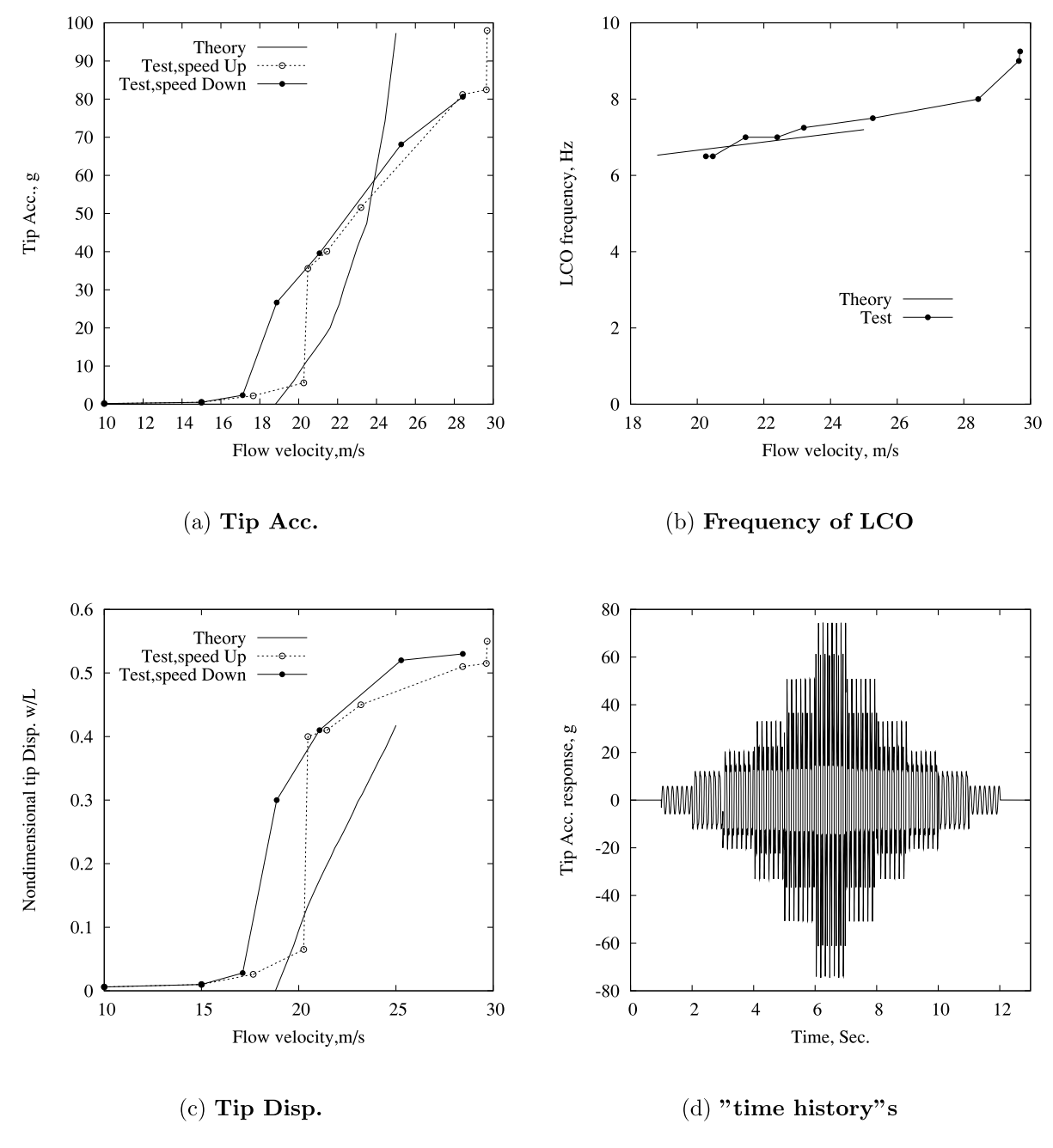


Fig. 13. Various responses vs. flow velocity, U, for the tip acceleration (a), LCO frequency (b), tip displacement (c) and theoretical "Time history" of acceleration for increasing and decreasing flow velocity (d).

4.2. Aeroelastic response and power extraction from flag flutter for partly covered model

Linear flutter analysis

The linear flutter calculations are based on a combination of the structural, aerodynamic and electric equations, Eqs. (9)–(11), when the structural and electric nonlinear forces are set to zero. For the linear vortex lattice aerodynamic model, the flag panel was modeled using 300 vortex elements. The total number of vortex elements (or aerodynamic degrees of freedom) was thus 600. The vortex relaxation factor was taken to be $\alpha=0.992$. For the structural model, five (5) bending modes are considered in the flutter calculations. The structural modal damping rate is taken as 0.015.

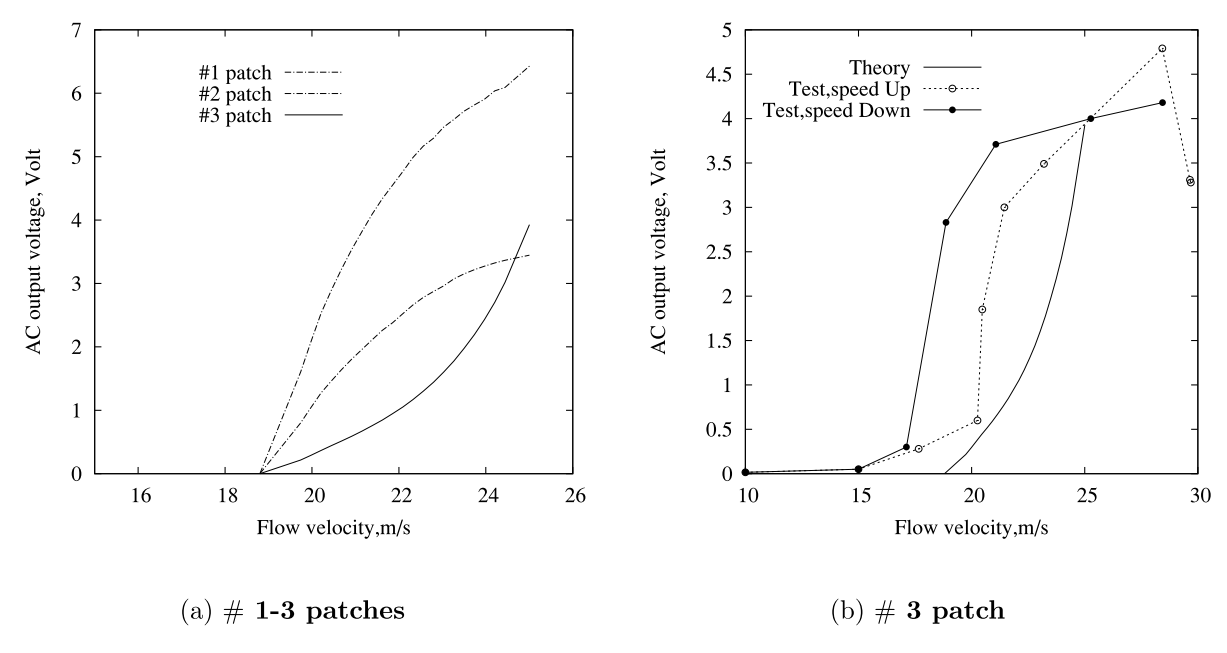


Fig. 14. The theoretical AC output voltage from # 1-3 patches (a) and # 3 patch for the theoretical and experimental correlation (b).

The aeroelastic eigenvalues obtained from these equations determine the stability of the system. When the real part of any one eigenvalue becomes positive (negative damping), the entire system becomes unstable.

Fig. 12 shows a typical graphical representation of the eigenanalysis in the form of the real part of the eigenvalues (damping ratio) vs the flow velocity (a) and also a root-locus plot (b). As indicated by the symbol \circ in Fig. 12(a), there is an intersection with the velocity axis at $U_f = 18.8$ m/s and the corresponding flutter oscillatory frequency in Fig. 12(b) is $\omega_f = 6.53$ Hz.

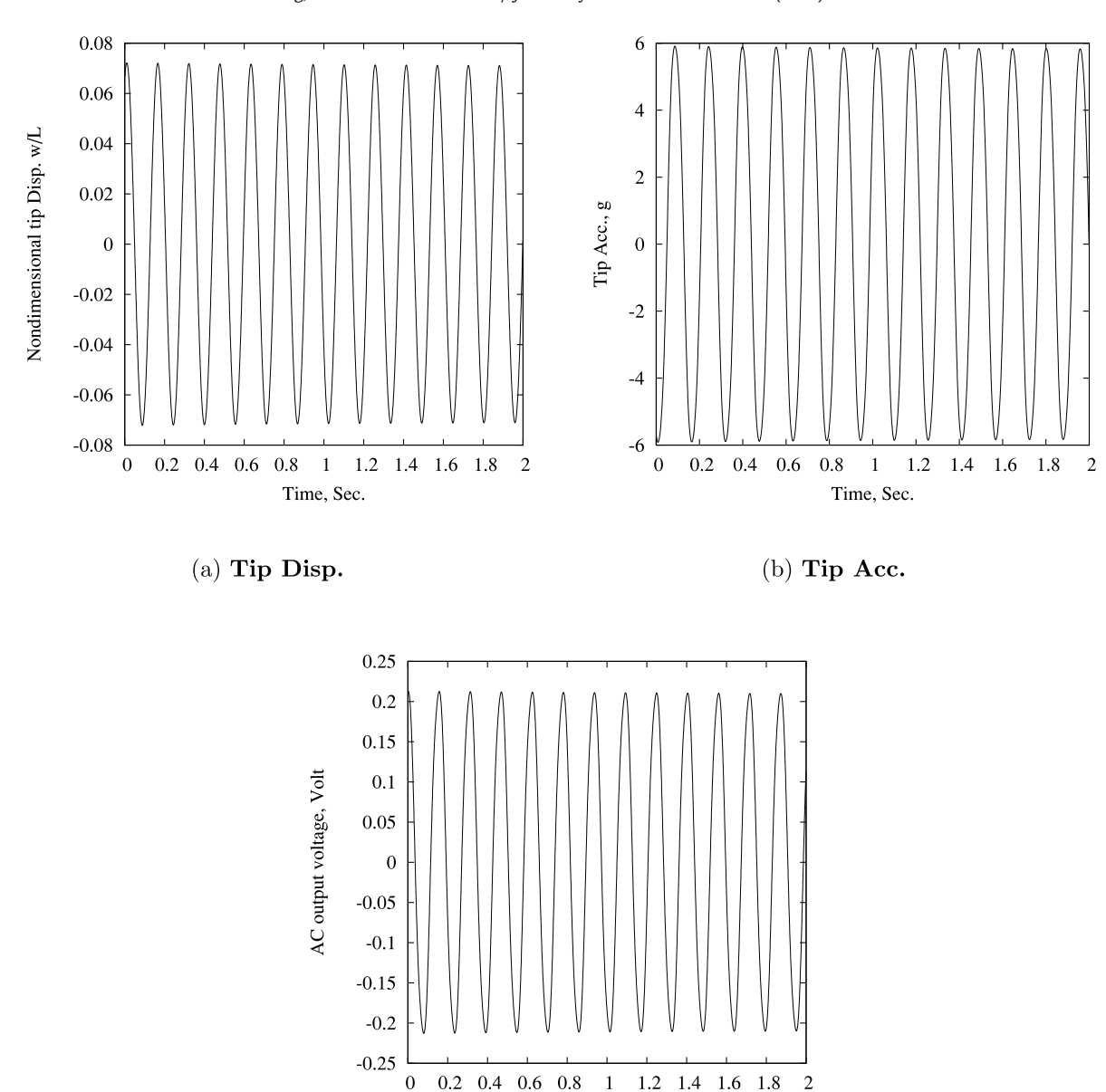
LCO response and power extraction

For the structural modal equation, the Runge–Kutta Fourth order algorithm is used and for the aerodynamic and electric network equations the finite-difference method is used to calculate the time history of the nonlinear response of this piezoelectric-aeroelastic system when the nonlinear forces, F_{BN} , F_{EN} and $A_{\dot{q},mn}$ are not zero. A peak nondimensional LCO amplitude (Disp.), w/L and acceleration amplitude (Acc.) divided by the gravity acceleration, peak output voltage and power extraction are used to represent the aeroelastic response and energy harvesting for comparison with the experimental results. Note that theoretical and experimental output voltages are obtained from a single piezo patch or a single film sensor on the side surface in the following discussions including the fully covered plate.

Fig. 13(a) shows the acceleration peak amplitude in g at the tip for flow speeds from 18.8 m/s to 25 m/s for the theory and 10 m/s to 29.7 m/s for the experiment. The theoretical tip acceleration as indicated by solid line rapidly increases as flow speed increases. For the experimental measurement, two different LCO responses for increasing and decreasing flow velocity were observed. The symbols, \circ plus broken line and \bullet plus solid line, indicate the experimental results for increasing and decreasing flow velocity, respectively. With increasing flow velocity, we find a jump at U = 20.6 m/s which is similar to the theoretical results at U = 18.8 m/s as shown by the solid line. As the flow velocity increases further, the LCO amplitude that is measured has a larger increase than that found from theory. When the flow velocity is decreased, we find another jump at U = 18.87 m/s as shown in Fig. 13(a) and as indicated by the symbol, \bullet with a solid line. The experimental linear critical flutter boundary is estimated from this figure. An intersection between the extrapolated LCO amplitude curve and the flow velocity axis is defined as the linear critical flutter boundary. The estimated experimental flutter velocity is 20.36 m/s and frequency is 6.4 Hz. Corresponding to the experimental acceleration peak response, the measured dominant LCO frequency are obtained. The theoretical and experimental LCO frequencies are shown in Fig. 13(b). The experimental LCO frequency is similar to the theoretical frequency.

From the measured dominant LCO frequency and acceleration peak amplitude, the peak displacement amplitude can be calculated. Due to loss of higher harmonic component in the acceleration response, the measured displacement amplitude may have an error. Fig. 13(c) shows the nondimensional tip peak amplitude vs the flow velocity. Similar to Fig. 13(a), two different LCO displacement responses are found for increasing and decreasing flow velocity. The correlation between the theory and experiment for displacement is perhaps not as good as compared to that for acceleration.

A hysteresis response was found in the experimental measurement, but not in the theoretical computations as shown in Fig. 13(d). Fig. 13(d) shows a "time history" of the theoretical LCO acceleration responses obtained from the increasing and decreasing flow velocity processes. There are eleven (7) flow velocities from U = 18.79 m/s to 24.4 m/s with $\Delta U = 18.79$ m/s with $\Delta U = 18.79$ m/s with $\Delta U = 18.79$ m/s with $\Delta U = 18.79$



(c) # 3 patch

Fig. 15. Time histories for the tip displacement, tip acceleration and output AC voltage from #3 patch for flow speed U = 19.7 m/s.

Time, Sec.

0.94 m/s for the increasing flow velocity. At each flow velocity, the time history is computed until the system achieves a steady state LCO response. The LCO response is shown in time intervals of one second for the these flow velocities. For the next flow velocity (increasing ΔU), we use initial conditions that are provided by the previous LCO state. This process is continuous in time until the flow velocity increases to U = 24.4 m/s. For the decreasing velocity process, six (6) flow velocities from U = 24.2 m/s to 18.79 m/s with the same velocity interval are used.

Fig. 14(a) shows the theoretical AC output voltage from the piezoelectric patches of P-876A12 # 1 to 3. Due to different positions in the x axis, the output voltages are different. Near the root of the plate, # 1 patch provides a higher AC voltage output and # 3 patch provides a lower AC voltage output. This is because the bending curvature velocity at #1 is larger than those at #2 and also # 3. Fig. 14(b) shows the correlation between the theoretical and experimental AC output voltage from the piezoelectric patch of P-876A12 # 3. Due to a hysteresis response in the experiment, the measured AC

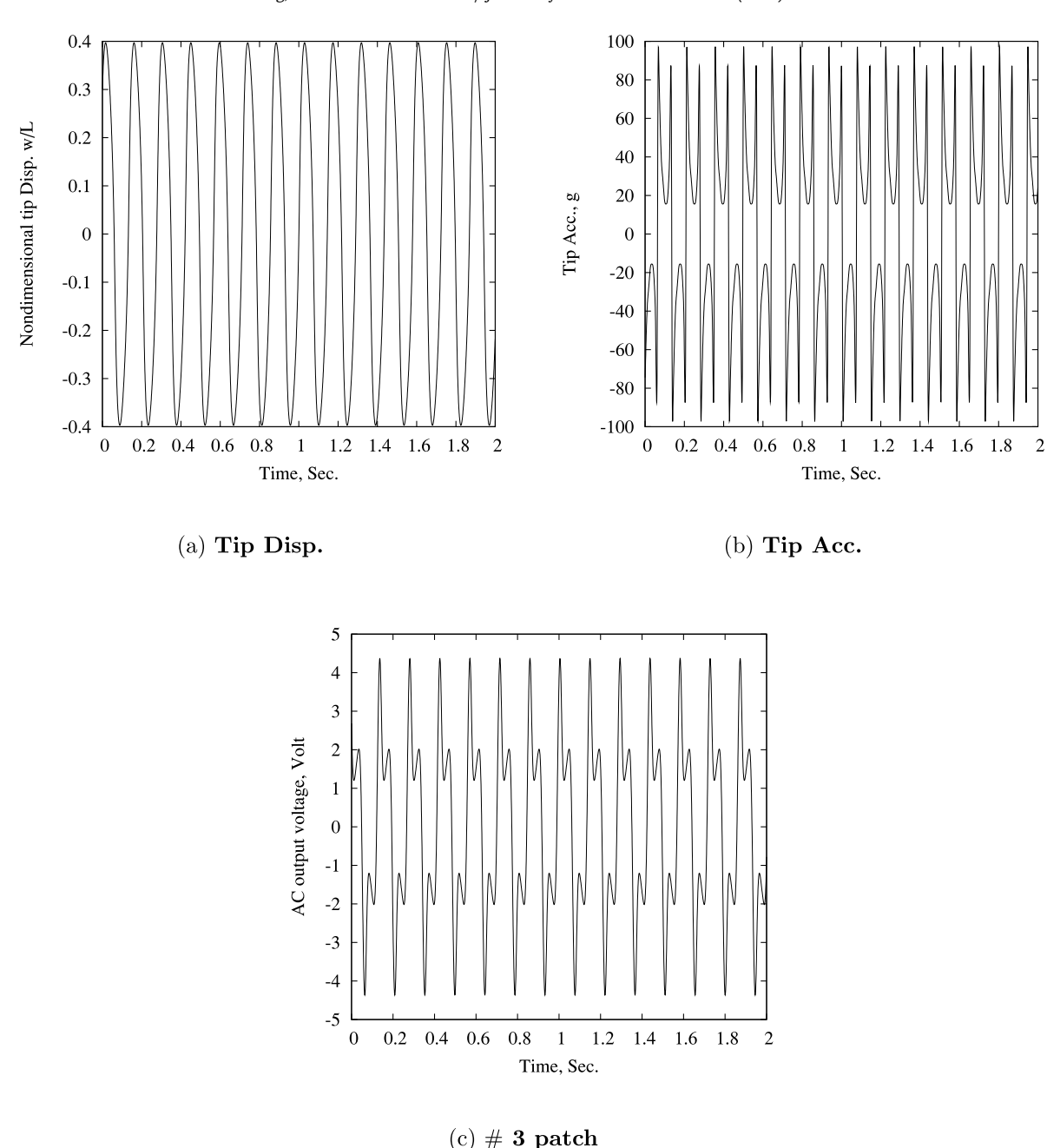


Fig. 16. Time histories for the tip displacement, tip acceleration and output AC voltage from #3 patch for flow speed U = 25 m/s.

output voltage has two different results for increasing and decreasing flow velocity. The theoretical results are closer to those from the experiment for increasing flow velocity than from the experiment for decreasing flow velocity.

Fig. 15 shows the time histories of the nondimensional tip displacement, tip acceleration and AC output voltage from # 3 patch for a small velocity, U = 19.7 m/s. It is found that the effect of structural nonlinearity is very small. These responses appear as a nearly sinusoidal motion. For the same case for a larger flow velocity, U = 25 m/s, the effect of the structural nonlinearity becomes larger as shown in Fig. 16. As shown in Fig. 16(a), there is a dominant LCO frequency. In addition to the dominant LCO frequency (near the flutter frequency), the response also includes a larger component at three (3) times the LCO frequency, $3\omega_{LCO}$. Fig. 17 shows the FFT analysis for above time histories for small, middle and large flow velocity. The dominant LCO frequency increases from 6.4 HZ to 7.1 Hz when the flow velocity increases from 19.7 m/s to 25 m/s. The higher harmonic component at $3 \times \omega_{LCO}$ frequency increases as the flow velocity increases. For

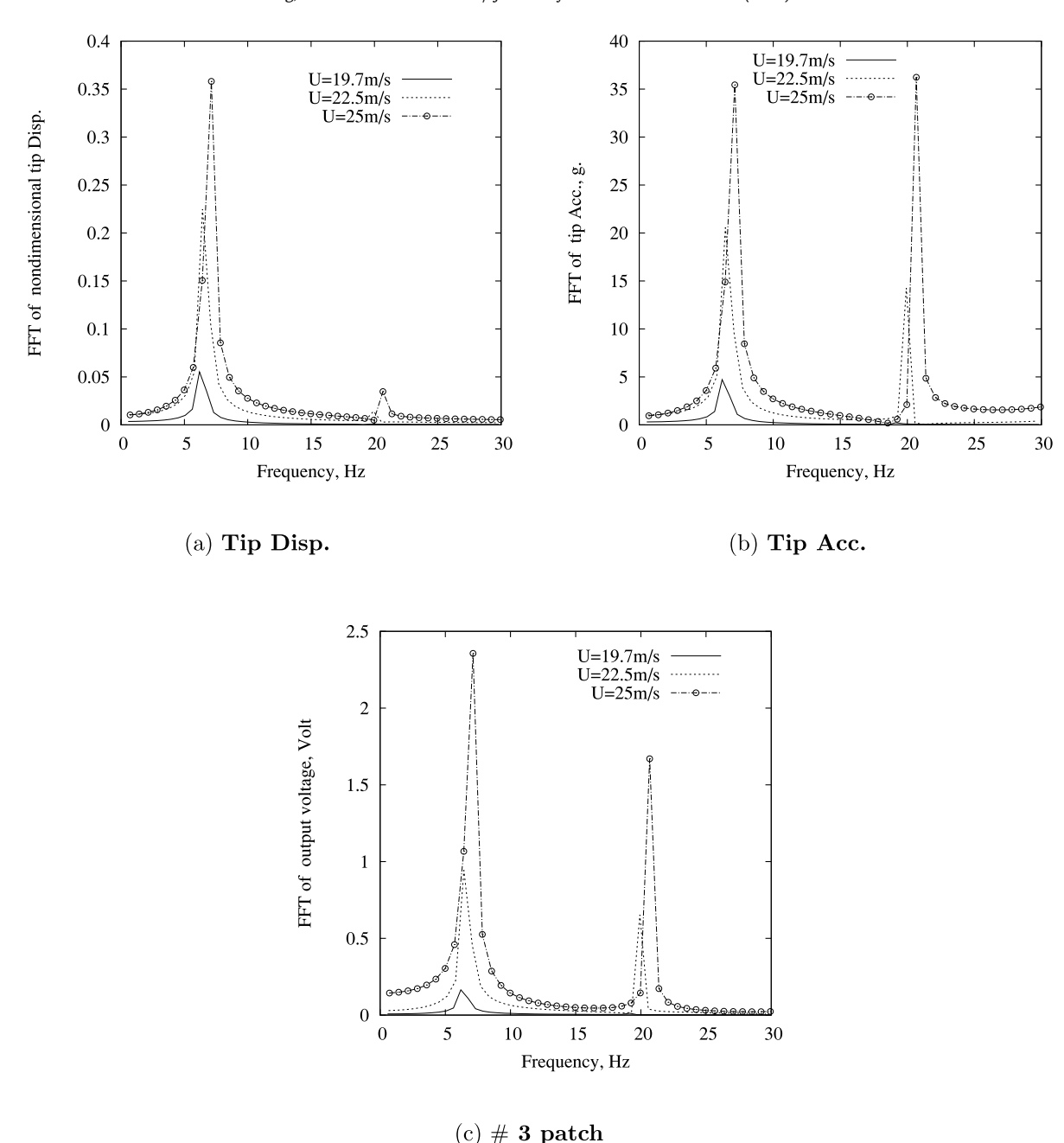


Fig. 17. FFT analysis of time histories for the tip displacement, tip acceleration and output AC voltage from #3 patch for flow speeds U = 19.7, 22.5 and 25 m/s.

the displacement response, the higher harmonic component is very small even at U=25 m/s. The higher component is only 10% of the dominant LCO component.

Now consider the theoretical LCO mode shape for both the displacement and acceleration responses. Fig. 18(a) shows the LCO displacement response for two different flow velocities, U = 19.7 and 25 m/s. The mode shapes are normalized to one at the tip. The broken line indicates the LCO mode for U = 25 m/s and solid line indicates the LCO mode for 19.7 m/s. For comparison, the first and second structural natural modes are also plotted in this figure as indicated the symbols, with a solid line and \circ with a broken line, respectively. For U = 19.7 m/s, the LCO mode shape includes 62% of first natural mode and 37% of second natural mode. For U = 25 m/s, the LCO mode shape includes 75% of first natural mode and 24% of second natural mode. Therefore, for both lower and higher flow velocities, the LCO modes are dominated by the first natural mode.

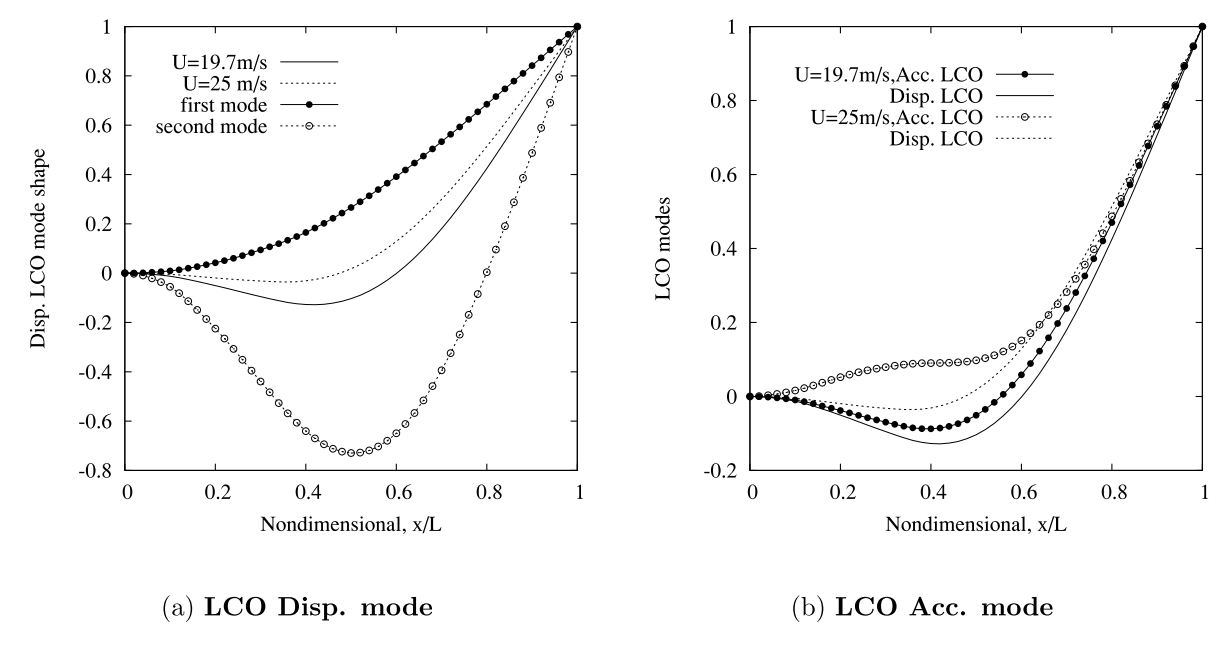


Fig. 18. LCO displacement modes and acceleration modes for flow speeds U = 19.7 and 25 m/s.

Fig. 18(b) shows the LCO mode of acceleration response for two different flow velocities of U=19.7 and 25 m/s. For comparison, the displacement LCO modes are also plotted in this figure. The broken line indicates the LCO mode for U=25 m/s and solid line indicates the LCO mode for 19.7 m/s. The symbols, • with a solid line and • with a broken line, indicate the acceleration LCO modes for U=19.7 and 25 m/s, respectively. For U=19.7 m/s, the acceleration LCO mode shape includes 68% of the first natural mode and 31% of the second natural mode and 0.5% of the third natural mode. For U=25 m/s, the acceleration LCO mode shape includes 73% of the first natural mode, 13% of the second natural mode and 10% of the third natural mode. Therefore, for both lower and higher flow velocities, the acceleration LCO modes are dominated by the first natural mode, but the third mode is not small.

Corresponding to the DC voltage outputs of # 3, P-876-A12 patch and the film sensors of # 4 and 6, the DC power extraction can be calculated as

$$P_{DC} = V_{DC}^2/R$$

where R is an effective resistance, R = 750 k Ohm. Fig. 19 shows the theoretical and experimental correlation of power extraction vs increasing flow velocity for patches # 3, 4 and 6. Considering the effect of experimental AC/DC converter on the power extraction, a reference power, ($P_{Ref.}$) concept is introduced. This is defined as

$$P_{Ref.} = V_{AC.test}^2 / R$$

This means the AC/DC converter has zero voltage drop, i.e no energy loss in the convert process. Thus, $P_{DC} = P_{Ref.}$. Here $V_{AC,test}$ is the measured AC voltage output. This reference power, "Ref. power", is indicated in the figure. The electric power extraction increases as the flow velocity increases as expected. Film sensor # 6 provides much lower power extraction than patch # 4 although they are both film sensors. This is because # 6 patch is near the beam tip and the bending curvature velocity at #6 is smaller than those at #4 and also # 3. Piezo patch # 3 provides much larger power extraction than patch # 4. This is because # 3 patch has a larger electric-mechanical coupling coefficient, e_{31} , than those of film sensor although the bending curvature velocity at # 3 is smaller than those at # 4. It is also found that the theoretical results are closer to the "Ref. power" results, i.e. the experimental results when the non-ideal experimental AC/DC converter is neglected.

4.3. Aeroelastic response and power extraction from flag flutter for fully covered model

Structural natural frequencies, modes and linear flutter analysis

As shown in Fig. 3 of the fully covered model by the film sensors, DT4-028 K/L, the aeroelastic model is considered as a uniform flag plate. The structural natural frequencies and mode shapes can be calculated for a uniform cantilevered beam. The experimental first natural bending frequency is $f_1 = 1.44$ Hz. The beam mass per length of the fully covered model is

$$\bar{m} = \rho_s b t_s + 8 \rho_t b_t b_s$$

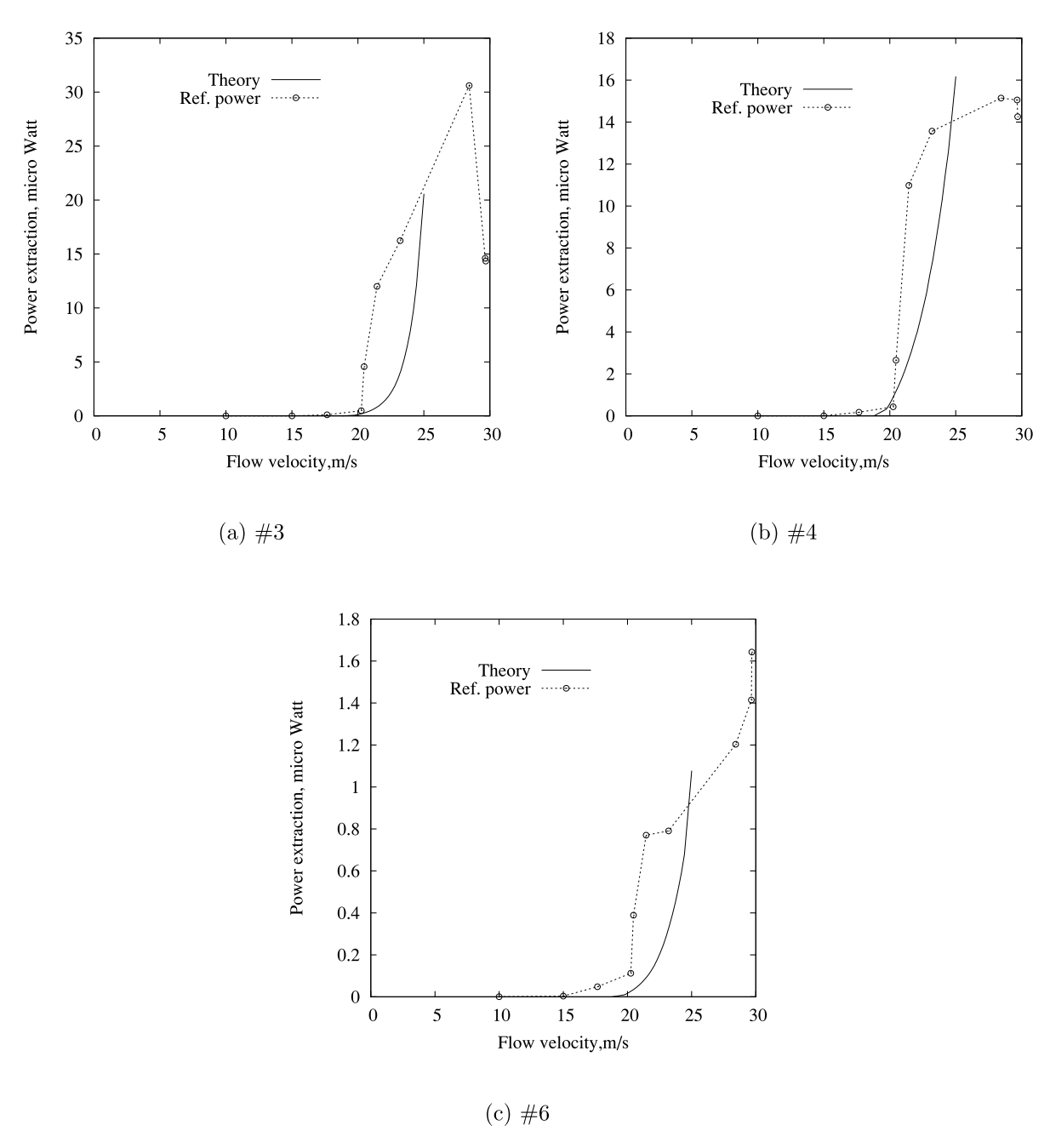


Fig. 19. Power extraction from piezoelectric patch at #3 (a) and piezo film sensors at #4 (b) and #6 (c).

Thus, the bending stiffness of the beam model, EI is determined using the experimental natural frequency, 1.44 Hz. It is

$$EI = \bar{m}(2\pi f_1)^2 L^4 / (1.875)^4$$

The theoretical first five (5) bending natural frequencies are 1.44, 9.02, 25.27, 49.5 and 81.86 Hz. The cantilever beam bending natural mode function is

$$\phi(x) = \cosh k_i x - \cos k_i x - \alpha_i (\sinh k_i x - \sin k_i x) , \quad \alpha_i = \frac{\cosh k_i L + \cos k_i L}{\sinh k_i L + \sin k_i L}$$

The linear flutter calculations for the fully covered model are based on a combination of the structural, aerodynamic and electric equations, Eqs. (9)–(11), when the structural and electric nonlinear forces are set to zero. All parameters for

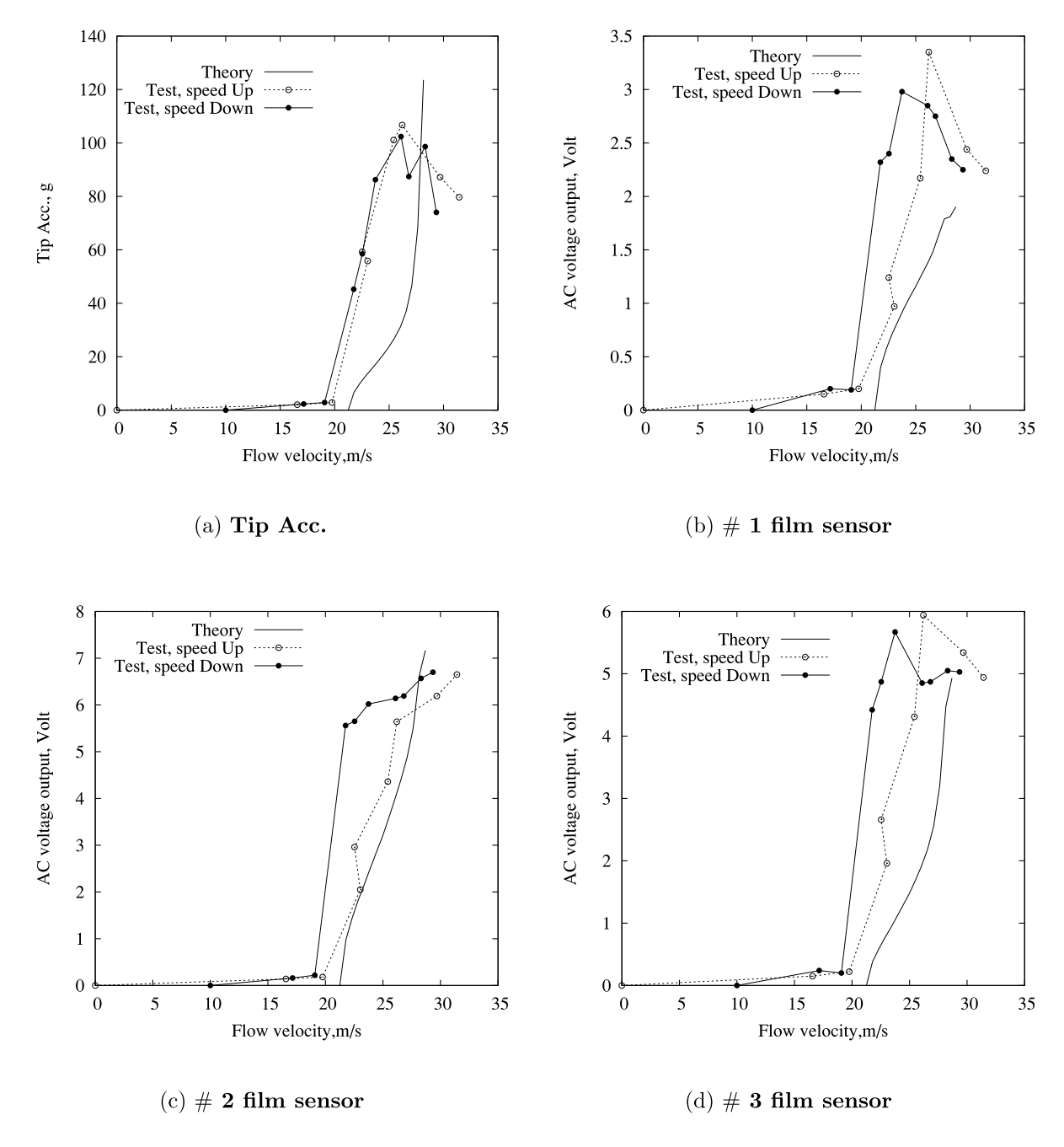


Fig. 20. Peak amplitudes vs. flow velocity for the tip acceleration (a), the theoretical and experimental AC output voltage from # 1 (b), # 2 (c) and # 3 (d).

the linear vortex lattice aerodynamic model are the same with those for the partly covered model. Five (5) bending modes are considered in the flutter calculations. The structural modal damping rate is taken as 0.015.

As indicated by the symbol \bullet in Fig. 12(a) for the fully covered model, there is an intersection with the velocity axis. The theoretical linear flutter speed and frequency are $U_f = 21.25$ m/s and $\omega_f = 6.24$ Hz.

LCO response and power extraction

The theoretical computations for the fully covered plate are similar to those for the partly covered plate for the non-linear structural modal and linear electric and aerodynamic equations. The same algorithm and aerodynamic parameters are used.

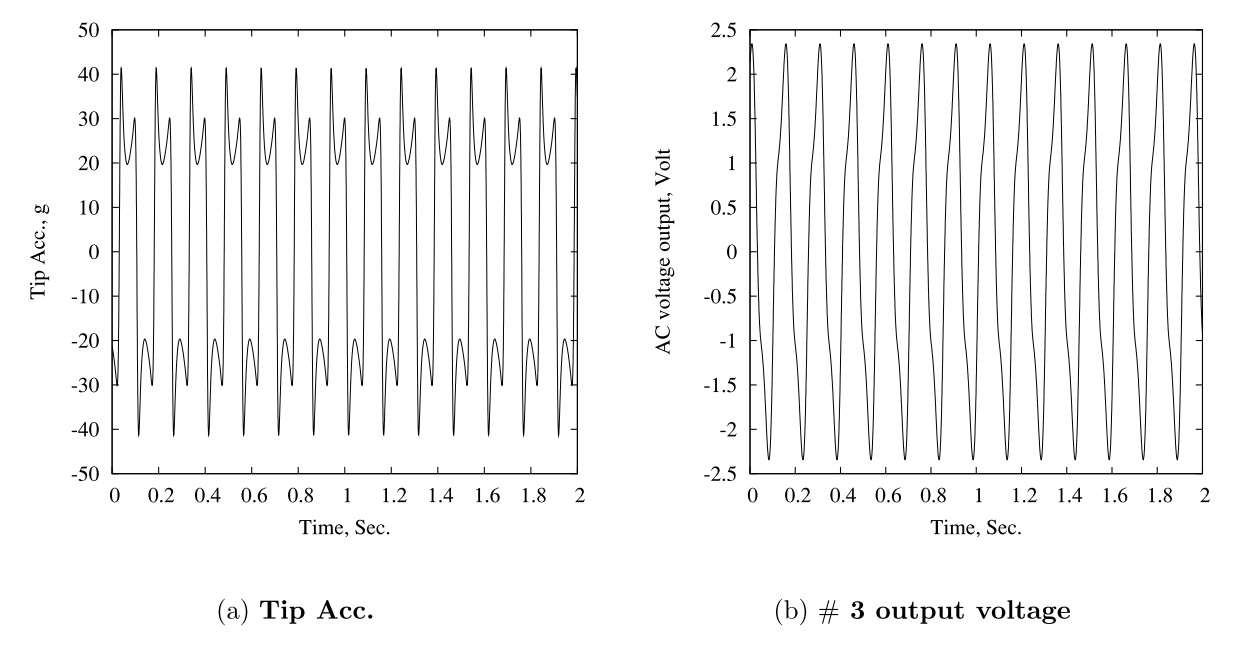


Fig. 21. Time histories for the tip acceleration (a) and output AC voltage from #3 (b), for flow speed U = 26.56 m/s.

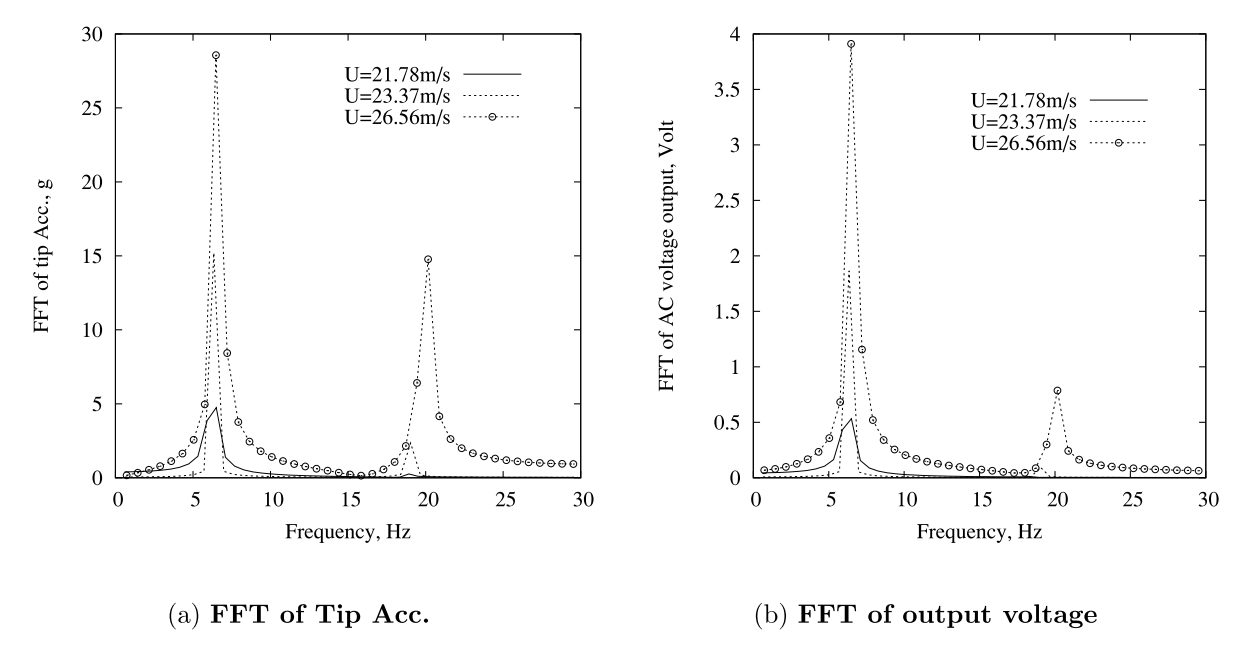
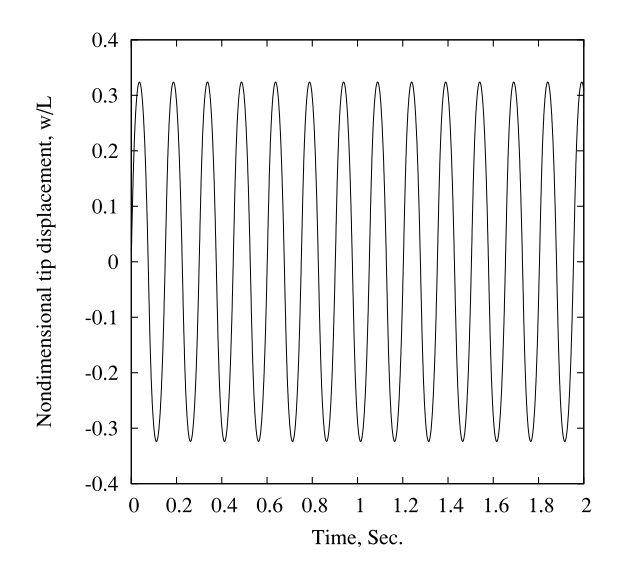
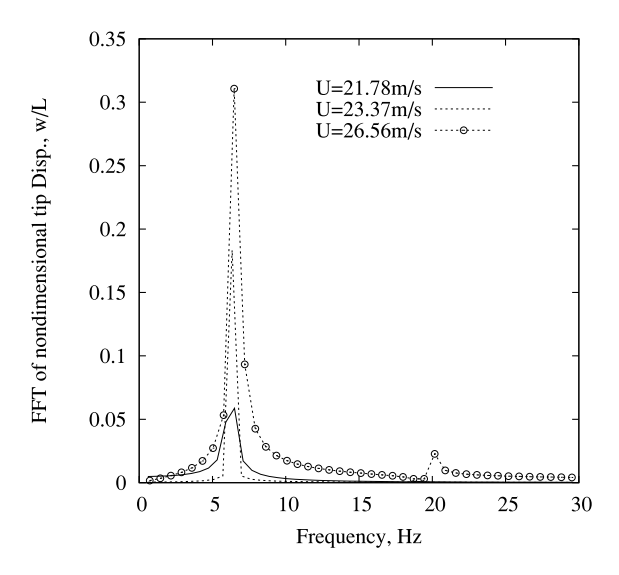


Fig. 22. FFT analysis of the tip acceleration (a) and output AC voltage from #3 (b) for flow speeds U = 21.78, 23.37 and 26.56 m/s.

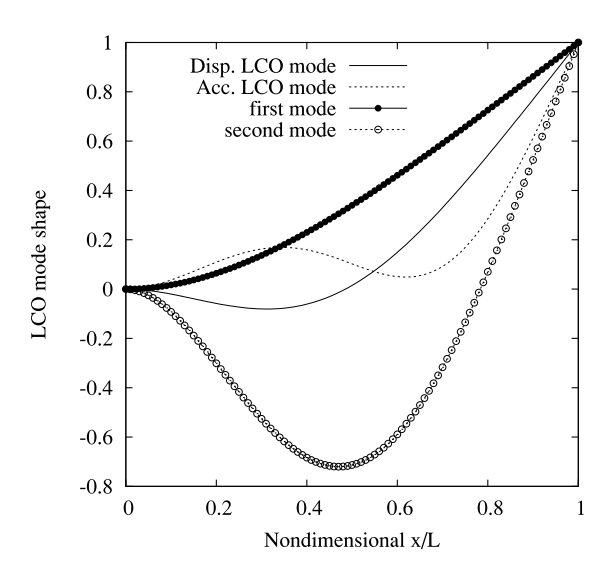
Fig. 20(a) shows the acceleration peak amplitude in g at the beam tip for flow speeds from 19.27 m/s to 28.15 m/s. The theoretical tip acceleration as indicated by solid line rapidly increases as the flow speed increases. For the experimental measurement, two different LCO responses for increasing and decreasing flow velocity were observed. The symbols, \circ plus broken line and \bullet plus solid line, indicate the experimental results for increasing and decreasing flow velocity, respectively. With increasing flow velocity, we find a jump at U = 23.03 m/s which is similar to the theoretical results at U = 23.03 m/s as shown by the solid line. As the flow velocity increases further, the LCO amplitude measured has dropped down, but the theoretical LCO amplitude continues to increase. This drop down phenomenon in the experiment may be created by a effect similar to that of a nonlinear stalled airfoil because of the large flag motions. When the flow velocity is decreased, another jump range from U = 21.7 m/s to 19.1 m/s was found as shown in Fig. 20(a) and as indicated by the symbol, \bullet





(a) Time history of tip response

(b) FFT of LCO tip Disp.



(c) LCO Disp. and Acc. modes

Fig. 23. Time history of tip displacement (a), FFT analysis of tip displacement and acceleration modes (c) at flow speed U = 26.56 m/s.

with a solid line. The experimental linear critical flutter boundary is estimated from this figure. The experimental flutter speed and frequency are 20.36 m/s and 7.25 Hz. The correlation is reasonably good.

Fig. 20(b)–20(d) show the theoretical and experimental AC output voltage from the film sensors, DT4-028K/L at # 1 and # 3. Due to different positions in the x axis, the output voltages are different. Near the root of the plate, # 1 film provides a lower AC voltage output and # 2 patch provides a higher AC voltage output. This is because the bending curvature velocity at #2 is larger than those at #1 and also at # 3. Due to hysteresis, the measured AC output voltage has two different results for increasing and decreasing flow velocity. The theoretical results are closer to those from the experiment for increasing flow velocity than from the experiment for decreasing flow velocity.

Fig. 21 shows the time histories of the tip acceleration and AC output voltage from # 3 film for a velocity, U = 26.56 m/s. It is found that the effect of the structural nonlinearity is larger at this higher flow velocity. In addition to the dominant component created by the dominant LCO frequency (near the flutter frequency), the response also includes

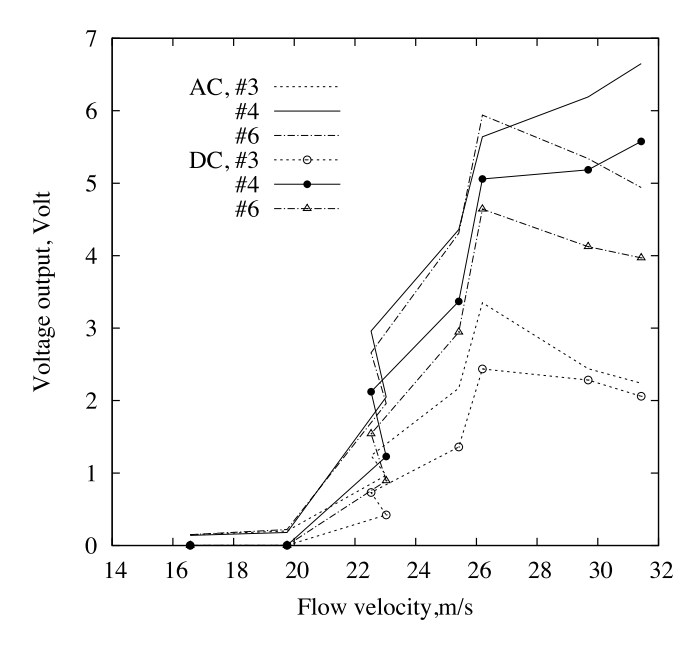


Fig. 24. Measured AC and DC voltage outputs of # 1-3 for increasing flow velocity.

a larger component at three (3) times the LCO frequency, $3\omega_{LCO}$. Fig. 22 shows the FFT analysis for above time histories for small, middle and large flow velocity. The dominant LCO frequency slowly increases from 6.34 HZ to 6.5 Hz when the flow velocity increases from 21.78 m/s to 26.56 m/s. The higher harmonic component response at $3 \times \omega_{LCO}$ frequency increases as the flow velocity increases.

Theoretical tip displacement vs the flow velocity is also calculated. A typical time history at U=26.56 m/s and corresponding of FFT analysis are shown in Fig. 23(a) and (b). For comparison, the FFT results for U=21.78 and U=23.37 m/s are also plotted in Fig. 23(b). Although, there is a larger effect of the structural stiffness nonlinearity on the acceleration response, the higher harmonic component is smaller than that of the dominant frequency. The displacement LCO is predominantly a single harmonic motion.

Fig. 23(c) shows the LCO modes of displacement and acceleration responses for a flow velocity of U=26.56 m/s. The broken line indicates the LCO mode for the displacement response and solid line for acceleration response. For comparison, the first and second structural natural modes are also plotted in this figure as indicated by the symbols, • with a solid line and \circ with a broken line, respectively. The displacement LCO mode shape includes 68% of first natural mode and 30% of second natural mode. The displacement LCO mode is dominated by the first natural mode. The acceleration LCO mode shape includes 54% of the first natural mode and 16% of the second natural mode and 25% of the third natural mode.

Fig. 24 shows the DC voltage output from the positions of # 1–3 of the film sensors for the increasing flow velocity. For comparison, the AC output voltages are also plotted in the same figure. There is a difference between AC and DC voltage. Corresponding to the DC voltage outputs, the DC power extraction can be calculated.

Fig. 25 shows the theoretical and experimental correlation of power extraction vs the increasing flow velocity for the film sensors of # 1–3. Considering the effect of experimental AC/DC converter on the power extraction, "Ref. power" is also plotted in this figure. The electric power extraction increases as the flow velocity increase as expected. The film sensor of # 2 provides much higher power extraction than the patches of # 1 and 3. This is because # 2 has the larger bending curvature velocity. The theoretical results are reasonably close to both the "Ref. power" and the real "Test" results.

Fig. 26(a) shows the total theoretical and experimental power extraction vs the increasing flow velocity for the fully covered plate. The fully covered plate has total 24 film sensors bonded to the substrate for both surfaces and each power extraction is based on a single film sensor. The total power extraction should be and is assumed to be the sum of each single film sensor and the results are shown in Fig. 26(a). The theoretical and experimental correlation is reasonably good. Fig. 26(b) shows the ratio in percent of the local power extraction from # 2 film sensors over the total power vs the increasing flow velocity for the theoretical and experimental correlation. More than half of the total power extraction comes from the film sensors at # 2 position. This means that it is very important to consider the optimal position of the piezo patch or film sensor.

5. Conclusions

Two experimental models of cantilevered plates, partially covered and fully covered respectively, by piezo patch and film sensors are constructed. Two different experimental methods are used; a force vibration experiment and a wind

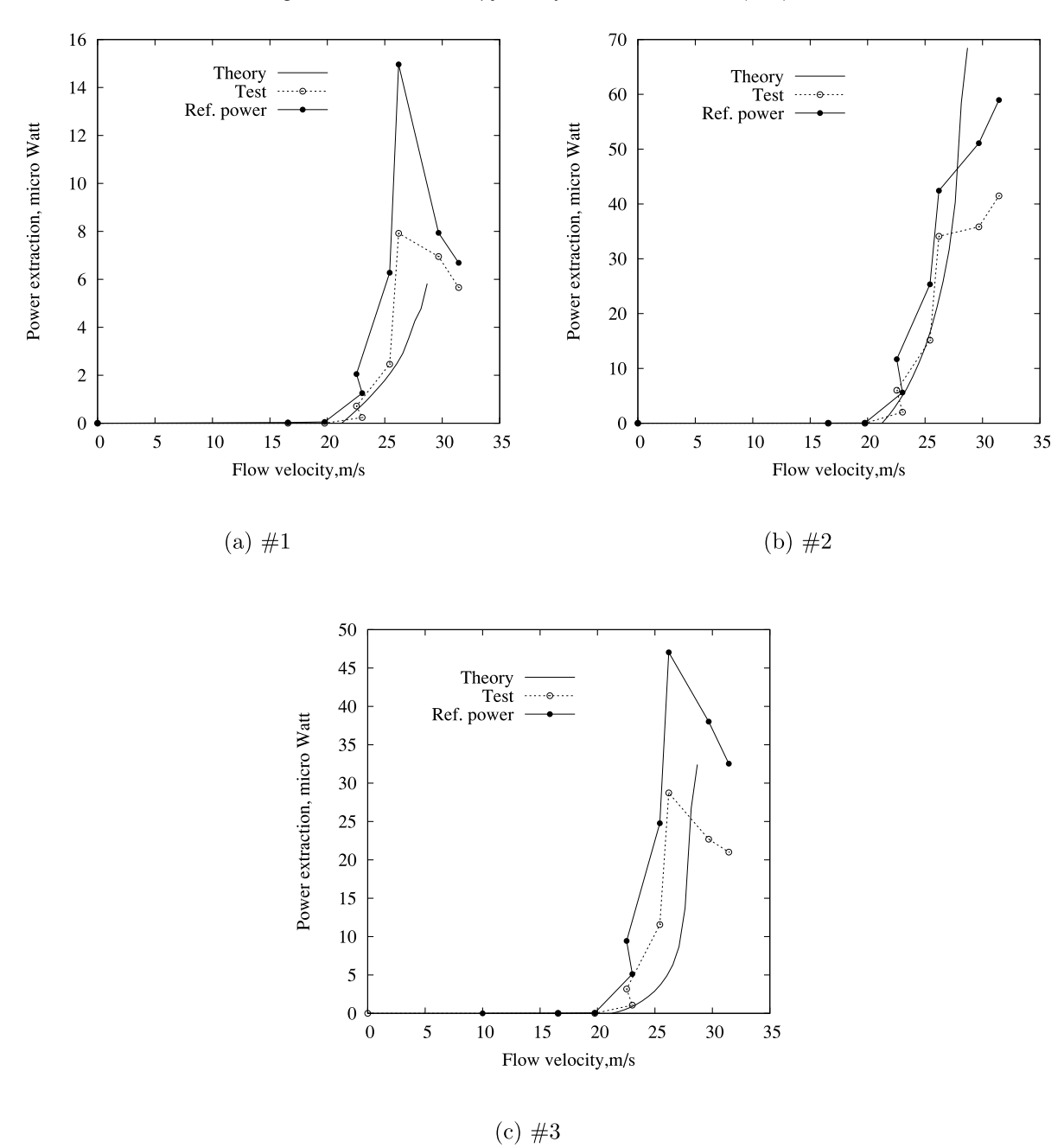


Fig. 25. Theoretical and experimental DC power extraction from film sensors at #1 (a),d #2 (b) and #3 (c) vs. increasing flow velocity.

tunnel experiment to obtain a large flapping vibrations. A DC power extraction through a AC/DC converter circuit is obtained. These experiments are used to evaluate a new computational model and code for a piezoelectric-aeroelastic system.

- 1. The inextensible beam theory has been verified by the dynamic force vibration test with larger flapping response. A good correlation between the theory and experiment was obtained for the structural motion.
- 2. A large LCO response beyond the linear flutter speed was observed from the wind tunnel experiment and correlated with results from the computational model for both experimental models. A good correlation for the linear flutter speed verifies that the theoretical linear piezoelectric-aeroelastic model is accurate. A reasonably good correlation for the LCO response shows the new computational code and the nonlinear inextensible beam theory is useful. A hysteresis response of LCO in the experimental measurement and amplitude drop down in the higher flow velocity were observed in the experiment, but not found in the computations.

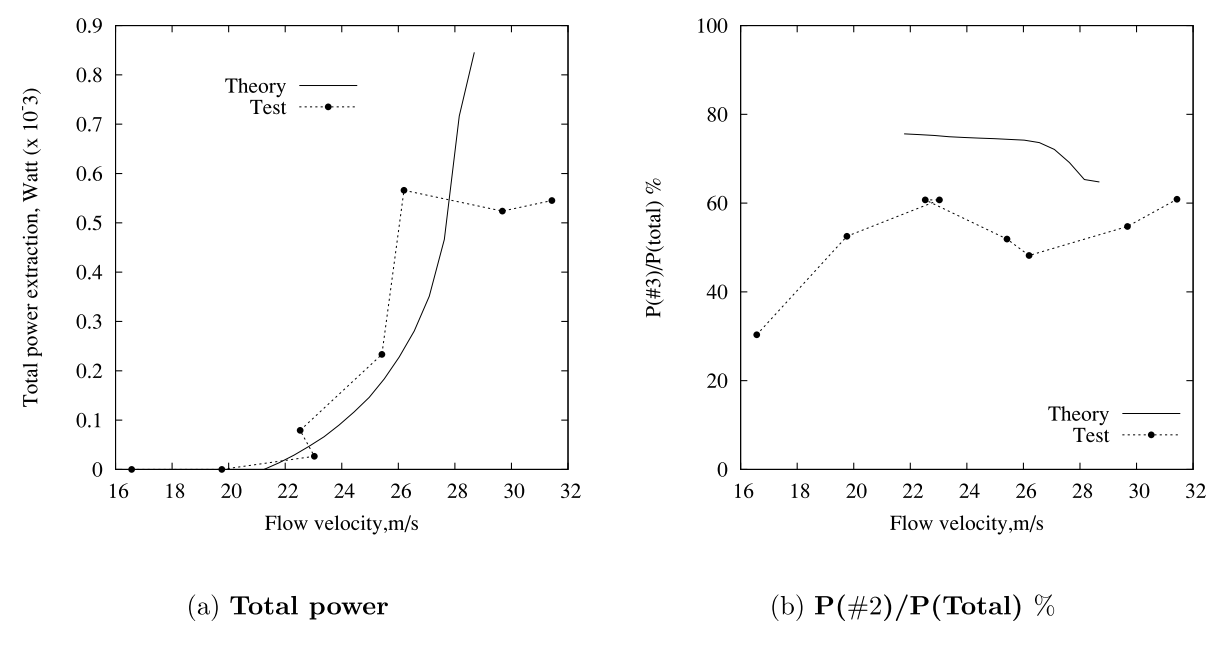


Fig. 26. Theoretical and experimental total DC power extraction (a) and local power at #2 over total power (%) (b) vs increasing flow velocity.

- 3. The displacement LCO response is a single harmonic motion, but the acceleration LCO response while dominated by the LCO frequency (close to the linear flutter frequency, ω_{LCO}) also has a detectable higher frequency at 3 ω_{LCO} due to the strong structural stiffness nonlinearity. The displacement LCO mode is dominated by the first natural mode and the acceleration LCO mode is dominated by the first and third natural modes.
- 4. The DC power extraction from the piezoelectric network equation depends on the dynamic vibration amplitude or the LCO amplitude as well as the LCO mode and the position of piezo patch or film sensor along the flow direction. This is because the best position with a larger bending curvature velocity provides a larger power extraction. Also the DC power extraction depends on AC/DC converter circuit and there is an opportunity for improvement in the experimental model in this respect.
- 5. Given the complexity of the interaction among the structural deformation, the aerodynamic flow field and the electrical field, the agreement between experiment and the computational model is in fact encouraging. The basic structural plus aerodynamic model has been studied by the authors and others and reported separately. See Tang et al. (2015). Not surprisingly, the added complexity of the electrical field leads to larger differences in the results between the experiment and the computational model compared to that of the aerodynamic plus structural model alone. However, it is clear that the basic physics of the experiment is being captured by the theoretical/computational model. But there is always room for improvement of course.

Acknowledgment

This work was supported in part by the National Science Foundation, USA under a program directed by Dr. Radhakisan Baheti and we are most appreciative of his enthusiasm and guidance for this work.

Appendix

$$P5_{ijkl} = \int_{0}^{L} EI(x) [\phi'_{x,i}\phi''_{x,j}\phi''_{x,k}\phi'_{x,l} + \phi''_{x,i}\phi'_{x,j}\phi'_{x,k}\phi''_{x,l}] dx$$

$$M^{b}_{ijkl} = \int_{0}^{L} m_{b}(x) [\int_{0}^{x} \phi'_{x,k}\phi'_{x,l}d\zeta \int_{0}^{x} \phi'_{x,j}\phi'_{x,i}d\zeta] dx$$

$$G1_{i,m} = \int_{x_{m}}^{x_{m}+l_{m}} \phi''_{x,i}$$

$$G2_{ijk,mn} = \int_{x_{m}}^{x_{m}+l_{m}} \phi''_{x,i}\phi'_{x,j}\phi'_{x,k}dx$$

Note that $\phi'_{x,i}$ indicate the derivative with respect to the structural coordinate (x).

References

Darmon, P., Benson, R.G., 1986. Numerical solution to an inextensible plate theory with experimental results. J. Appl. Mech. 53, 886–890. Dunnmon, J.A., Stanton, S.C., Mann, B.P., Dowell, E.H., 2011. Power extraction from aeroelastic limit cycle oscillations. J. Fluids Struct. 27 (8), 1182–1198. Kim, D., Cosse, J., Ceerdeira, C.H., Gharib, M., 2013. Flapping dynamics of an inverted flag. J. Fluid Mech. 736, R1. http://dx.doi.org/10.1017/jfm.2013.555. Li, D., Wu, Y., Da Ronch, A., Xiang, J., 2016. Energy harvesting by means of flow-induced vibrations in aerospace vehicles. Prog. Aerosp. Sci. Ryu, J., Park, S.G., Kim, B., Sung, H.J., 2015. Flapping dynamics of an inverted flag in a uniform flow. J. Fluids Struct. 57, 159–169. Simmonds, J.G., Libai, A., 1981. Exact equations for the large inextensional motion of plates. J. Appl. Mech. 48, 109–112. Stanton, S.C., Erturk, B.P., D.J. Inman, D.J., 2010. Nonlinear piezoelectricity in electroelastic energy harvesters: modeling and experimental identification.

stanton, S.C., Erturk, B.P., D.J. Inman, D.J., 2010. Nonlinear piezoelectricity in electroelastic energy harvesters: modeling and experimental identification
J. Appl. Phys. 108, 07903-1-07903-9.

Tang, Deman, Dowell, E.H., 2018. Aeroelastic response and energy harvesting from a cantilevered piezoelectric laminated plate. J. Fluids Struct. 76, 14–36.

Tang, D.M., Gibbs, S.C., Dowell, E.H., 2015. Nonlinear aeroelastic analysis with inextensible plate theory including correlation with experiment. AIAA J. 53 (5), 1299–1308.

Tang, D.M., Zhao, M.G., Dowell, E.H., 2014. Inextensible beam and plate theory: computational analysis and comparison with experiment. J. Appl. Mech. 81 (6), 061009.

Wang, X., Alben, S., Li, C., Young, Y.L., 2016. Stability and scalability of piezoelectric flags. Phys. Fluids 28, 023601. http://dx.doi.org/10.1063/1.4940990. Wang, Q., Wu, N., 2012. Optimal design of a piezoelectric coupled beam for power harvesting. Smart Mater. Struct. 085013.